# 15 Antireflective silicon nanostructures

*Young J. Yoo, Eun K. Kang, Yong T. Lee, and Young M. Song*

## Contents

## 15.1  INTRODUCTION

In optoelectronic devices or optical components, the suppression of surface reflections caused by discontinuity of the refractive index (RI) between two different optical media is crucial. For instance, the efficiency of a photovoltaic device is primarily limited by the Fresnel reflection loss on the surface of the device. Such a reflection loss is especially highlighted in materials with a high RI such as Si, GaAs, and GaP. Other optoelectronic devices, including light-emitting diodes (LEDs), laser diodes, and photodetectors, have similar problems [1,2]. A "ghost image" in glasses and other transparent materials is also generated by the Fresnel reflection loss [3]. Thin-film technology is commonly used for mass production of antireflection coatings (ARCs) with quarter wavelength stacks. However, it shows antireflection (AR) properties only in specific wavelength ranges and for limited incidence angles. Additionally, thin-film multilayers have problems with material appropriateness, thermal mismatch, and instability of the stacks [4].

Nowadays, the ideas of bionics have intruded into many technological fields. In the field of optical science and technology, a variety of biomimetic concepts, including photonic crystals in opals, vivid colors in butterfly wings, and deformable eye lenses in birds and mammals, have been developed [5–7]. A few decades ago, Bernhard and Miller discovered that the outer surface of facet lenses in the eyes of a moth consists of an array of cuticular protuberances termed "corneal nipples" [8]. A set of facet lenses of the insect's eye, the cornea, is approximately a hemisphere (Figure 15.1a). The convex outer surface of the facet lenses consists of the corneal nipples, which are locally arranged in a highly regular hexagonal lattice (Figure 15.1b and c) [9]. The optical action of the corneal nipple array is a severe reduction in the reflectance of the facet lens surface [10]. The operation of the moth-eye surface may be understood most easily in terms of a surface layer, in which the RI varies gradually from unity to that of the bulk material [11]. The insight that nipple arrays can significantly reduce the surface reflectance has been widely applied [12].

(a)                                    (b)                                    (c)

(d)                                    (e)
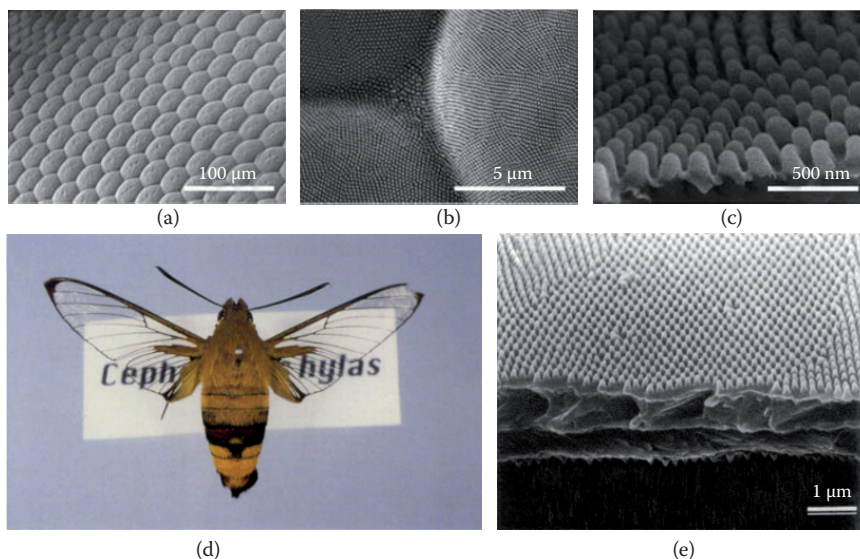
**Figure 15.1** Scanning electron micrographs of (a) the Attacus atlas moth eye showing the compound eye structure. (b) The nipple array in one facet lens. (c) The local arrangement of domains with highly ordered nipple arrays. (Reproduced from Ko, D.-H., et al., Biomimetic microlens array with antireflective ''moth-eye'' surface, *Soft Matter* 7 (2011), 6404, By permission of The Royal Society of Chemistry.) (d) A hawkmoth, *Cephonodes hylas*, male. The letters under the animal are visible due to the transparent part of the wing. (e) The SEM image of the oblique view of the rough wing with protuberances. (Reproduced from Yoshida, A., et al., Antireflective nanoprotuberance array in the transparent wing of a hawkmoth, *Cephonodes Hylas*, *Zool. Sci.* 14 (1997), 737–41, By permission of The Zoological Society of Japan.)

Closely packed nipple arrays can also be found in the wings of some moth species. The wings of adult *Cephonodes* are transparent except for small parts, that is, the wing margin and veins (Figure 15.1d). This transparent part has regular and hexagonal protuberances with no scales. The center-to-center distance between neighboring structures is about 200 nm, as shown in Figure 15.1e. Protuberances are dome- or nipple-shaped and have a constriction around their middle height [13]. Similar nipple arrays have also been observed on the wings of cicadas, which can be used for producing superhydrophobic surfaces for water-repellent applications [14,15].

To overcome the limitation of multilayer structures, the biomimetic optical concept of the moth eye and effective media has been transferred into the technological world within the past decades. The interest in tapered subwavelength gratings was also driven by the new possibilities of numerical simulation and of micro and nanofabrication. Moreover, highly efficient optical devices with such moth-eye structures were reported. In this chapter, we begin by explaining the basic principles of the optic behavior in the moth-eye structures and other graded index media. Several fabrication techniques, including top-down, bottom-up, and soft molding, for creating antireflective nanostructures are discussed. Examples of silicon-based optoelectronic devices illustrate the power of these concepts. We also discuss design guidelines and parametric studies for specific optoelectronic devices.

## 15.2 THEORY OF ANTIREFLECTIVE NANOSTRUCTURES

For traditional layered ARCs widely used in many optical and optoelectronic devices, the basic principle of a single-layer dielectric thin film with a low RI ($n$) on a substrate with a different RI ($n_s$), where $n_s > n$, follows the film interference law. Two interfaces are generated in the thin-film configuration, which produces two reflected waves, and destructive interference occurs when these two waves are out of phase. The minimum reflection loss can be achieved for the optimized thickness and RI of an ARC, which are dependent on the wavelength, angle, and polarization of incident light. Therefore, single-layer ARCs can only obtain

a high AR performance toward incident light under specific conditions, that is, wavelength, incidence angle, and polarization [16–18]. ARCs based on micro and nanostructure arrays follow an alternative way of reflectance reduction. Depending on the characteristic scale of the structures, two different ways of the interaction between the arrayed structures and incident light exist [17–19]. If the size of an individual unit is much larger than the wavelength, namely, a macrostructure unit, incident light is reflected normally and scattered after being absorbed partly. If the depth and the space between individual structural units are on the same scale as the light wavelength, light rays are trapped in the gaps leading to multiple internal reflections [20,21]. Thus, incident radiation can be absorbed reducing the reflection in the visible range to a very low level. The amount of the reflection is strongly dependent on the geometry of the structures.

On the contrary, when the AR structures have dimensions less than the wavelength, that is, located in the subwavelength scale or nanoscale, an alternative means is employed. If the AR surface has a gradient RI, light is insensitive to the AR structures and tends to bend progressively [22,23]. Even though the angle of incidence is changed, the coating still exhibits a relatively smooth change in the RI toward the incident direction of light, suppressing the reflection of light for a broad range of the wavelength [20,22]. Moreover, natural light always shows some degree of polarization, including s- and p-polarizations, which have the electric field perpendicular and parallel to the incidence plane, respectively. For the subwavelength-scale or nanoscale arrays with a smoothly graded RI from air to a substrate, the reflection of light with either s- or p-polarization can be suppressed to a very low level because the transmission of light with different polarizations is insensitive to media with extremely low disparity of the RI. Therefore, this type of ARCs based on nanostructure arrays with a gradient RI can realize broadband, omnidirectional, and polarization-insensitive AR performance, which is superior to that of layered ARCs.

Generally, different nanostructure arrays may have different RI profile curves, such as linear, parabolic, cubic, quintic, exponential, and exponential–sinusoidal curves, exhibiting different AR performances [21,24]. Theoretical computation is important in developing and optimizing high-performance AR surfaces. In the view of the effective medium theory (EMT), which is an essential concept for many computational models in the area of antireflectivity, the surface RI depends on the topology and the composition and can be calculated as a function of the volume fraction of inclusion for a material mixture [17,18,25–27]. As for a nanostructure array film, the effective RI can be determined by considering the surface consisting of layers of homogeneous mixtures of nanostructured materials and the air in the interspaces. The rigorous coupled-wave analysis (RCWA), first proposed by Moharam and Gaylord in 1981, is widely used in the theoretical calculations to optimize the ARC design [28]. This analytical model is a relatively straightforward technique to exactly solve Maxwell's equations to accurately analyze the diffraction of electromagnetic waves. In the RCWA, the cross-section of the structures is treated as consisting of a large number of thin layers parallel to the surface. A particular formulation without any approximations has been developed to analyze both transmission and reflection from planar and surface-relief structures accurately and efficiently. Using this model, the performance of AR structures can be predicted and the structure optimization of ARCs can be conducted.

As illustrated in Figure 15.2, ARCs can be classified into two basic types: those based on inhomogeneous layers and those that consist of a homogeneous layer [29,30]. A single inhomogeneous layer with RI $n_m$ on a substrate with RI $n_s$ at a wavelength $\lambda$ has an optical thickness equal to $\lambda/4$ and the RIs satisfy the relation $n = \sqrt{(n_s n_m)}$ (Figure 15.2a). However, these conditions can be satisfied only at a specific wavelength because of material dispersion. Double-inhomogeneous layers have a medium with a lower RI on the bottom coating layer (Figure 15.2b). Although the two-step change of the RI from air to the substrate can reduce the reflection, discontinuity of the RI at each layer remains. Finally, multi-inhomogeneous layers have a graded index, indicating a smooth change in the RI of each layer. By the use of multiple thin-film layers, zero reflectance can be obtained at one or more wavelengths even if the RI relationship given above is not satisfied (Figure 15.2c). A lower effective index $n$ of the homogeneous layer is achieved when the layer is patterned or structured. A homogeneous porous layer acts like a single inhomogeneous layer because a porous pattern without tapering means invariance of the effective index along the depth of the patterned layer (Figure 15.2d). A tapered porous layer has a graded index profile; however, the effective index of the layer changes abruptly at the end of the structure, causing a reflection loss at the surface (Figure 15.2e).
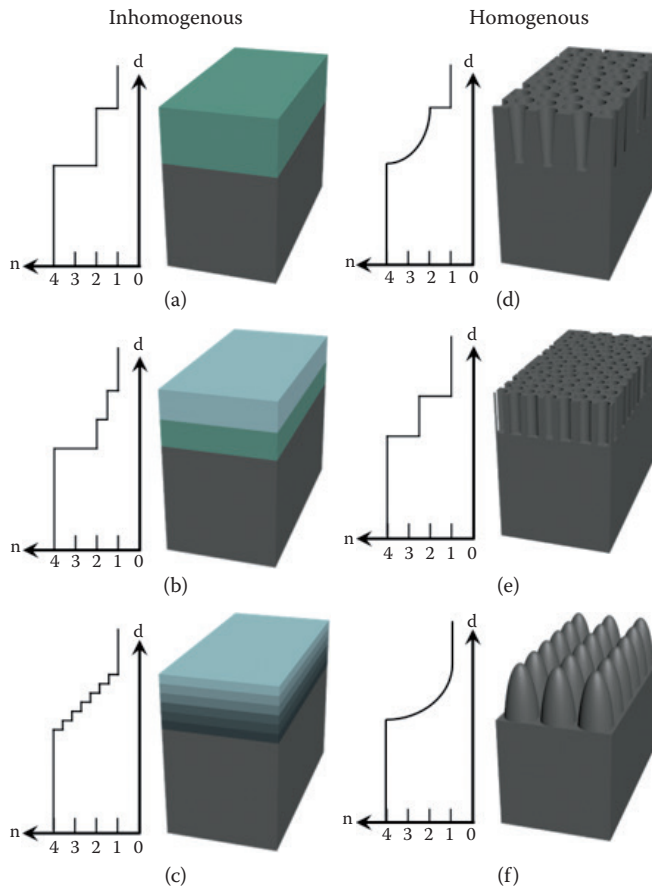
**Figure 15.2** Structure and effective RI profiles of various types of ARCs. (a)–(c) Inhomogeneous single-layer, multilayer, and graded-index ARCs and (d)–(f) homogeneous porous, tapered porous, and moth-eye ARCs.

A smooth change in the effective RI can be achieved by introducing artificial moth-eye structures, provided that its thickness exceeds at least one or two waves and that the lateral dimensions of the patterns are less than the light wavelength (Figure 15.2f). When these conditions are satisfied, the EMT can be applied and the material–air structure can be represented by a series of thin films with RIs that vary gradually from unity (air) to $n_s$, the substrate index.

A perfect ARC should meet the requirements of excellent AR properties, namely, broadband, omnidirectional, and polarization-insensitive antireflectivity [17,18]. The fact that there may be a difference in RI matching or optical impedance matching required for different wavelength regions, such as visible, ultraviolet (UV), and near-infrared regions, impairs the broadband AR performance of ARCs. The incidence angles have a significant impact on the reflectance. For example, most glass and plastics with an RI of ~1.5 exhibit a reflectance of 4% at normal incidence, but a much higher reflectance, even a reflectance of 100%, can be reached as the incidence angles are increased [17,18]. This causes difficulties in the case of solar cells that should be mechanically oriented to face the sun throughout the day, which needs additional control devices and energy consumption. Therefore, omnidirectional antireflectivity is important for the practical applications of ARCs in photovoltaic modules. Moreover, ARCs have to be insensitive to the light polarization because at smaller angles, p-polarized light is maximally reflected. Therefore, a perfect antireflective coating should exhibit broadband, omnidirectional, and polarization-insensitive antireflectivity. A traditional layered AR film has difficulties with satisfying all the requirements because of the fundamental interference destructive principles. There has been considerable progress toward perfect ARCs based on nanostructure arrays in recent years.

# 15.3 ARTIFICIALLY ENGINEERED MOTH-EYE STRUCTURES

## 15.3.1 QUARTER-WAVELENGTH ARC AND MULTILAYER ARC

The AR performance of traditional quarter-wavelength ARCs depends on the coating thickness and the material RI. Careful control of both factors would result in lowering the amount of the reflection from the surface [31,32]. As mentioned in Chapter 2, optical reflection can be efficiently suppressed if the RI of the coating material is equal to the geometric mean of the RIs of the two media at the interface [33]. A quarter-wavelength coating will allow light reflected from the surrounding medium/ARC interface and the ARC/substrate interface to interfere destructively, eliminating the reflection. The amount of the reflection also depends on the angle of the incident light [24,34]. Numerous methods of quarter-wavelength ARC production have been developed, for example, vacuum-based deposition processes and layer-by-layer deposition of polyelectrolyte and/or nanoparticle films [31].

A limited number of materials with an adequate RI (generally for low-RI substrates) are one of the major limitations of single-layer coating. The use of composite single-layer ARCs, whose RI can be tuned by changing the ratio (filling factor) of the constituents of the composite, is one of the solutions to this problem. As shown in Figure 15.3a, mesoporous silica nanoparticles are used for fabricating antireflective coatings on glass substrates [35]. The combination of mesoporous silica nanoparticles in conjunction with a suitable binder material allows mechanically robust single-layer coatings with a reflectance of <0.1% to be produced by using simple wet-processing techniques (Figure 15.3b). Further advantages of these films are that their structure results in antireflective properties with a minimum reflection that can be tuned between 400 and 1900 nm. The ratio of the binder material to mesoporous nanoparticles allows the RI control [35]. Double-layer ARCs are also widely used for reflection reduction. In the case of double-layer ARCs, the upper film facing air usually has the lowest RI and another layer is made successively based on the ascending order of their RIs. Similar to single-layer coating, the interference conditions should be fulfilled to destructively cancel bouncing back waves off the substance surface. Hence, the thickness of each layer is usually a quarter or half of the wavelength. Similar to single-layer ARC, each layer of a double-layer configuration can be made of a composite material with a tunable RI to provide more design flexibility [36]. The AR in a wide wavelength range originates from a reasonable RI gradient from air to the substrate produced by mesopores in the bottom-layer silica coating and particle-packed pores in the top-layer silica coating (Figure 15.3c and e). The maximum transmittance of the broadband ARC was approximated to 100.0% at the peak value and above 99.6% in the visible region from 400 to 800 nm. Meanwhile, the average transmittance of the coating was more than 99.0% over the range of 360–920 nm (Figure 15.3d). In addition, the double-layer broadband silica ARC showed a considerable mechanical performance and a high environmental stability [37].

## 15.3.2 GRADED-INDEX ARC

A gradual change in the film RI from the substrate RI ($n_s$) to the air RI ($n_{air}$) is an alternative way of reflectance reduction. Interference effects in the stacking layers of a dielectric rely on multipass light circulation inside the optical media formed by the films [36,38]. This means that the reflection of a multilayer coating strongly correlates with the thickness and RI of each layer. Nanostructured multilayers for graded-index ARC are achieved using oblique-angle deposition [39,40]. Oblique-angle deposition provides the control on the thin-film porosity and thickness, resulting in consistency of the ARC design parameters with actual parameters [41,42].

Figure 15.4 shows several examples of multilayered gradient media for broadband AR characteristics [43–45]. For instance, a three-layer graded-index ARC to Si is composed of the following layers: the first layer of $TiO_2$ ($n$ = 2.66 at 550 nm), the second layer of $SiO_2$ ($n$ = 1.47 at 550 nm), and the third layer of low-$n$ $SiO_2$ ($n$ = 1.07 at 550 nm) (Figure 15.4a). The first layer of $TiO_2$ and the second layer of $SiO_2$ are deposited by means of reactive sputtering. The third layer of porous $SiO_2$ is deposited using the oblique-angle e-beam evaporation technique (Figure 15.4b). The desired low RI is achieved by mounting the sample such that the substrate normal is at 85° to the incoming flux. By averaging over the wavelength range from 400 to 1100 nm and the incidence angle range of 0°–90°, it is found that polished Si reflects ~37% of

(a)

(b)

(c)

(d)

(e)
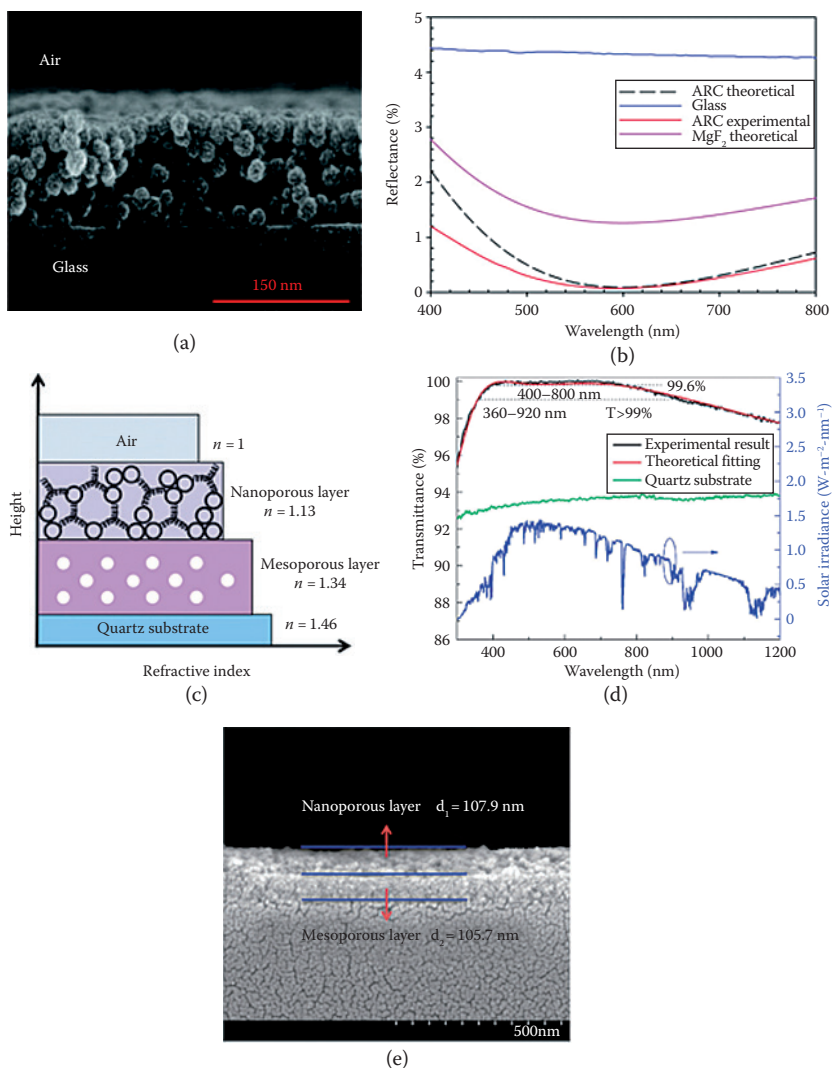
**Figure 15.3** (a) Cross-sectional SEM image of a single-layer silica ARC on a glass substrate. (b) The experimental reflection spectra of glass and the ARC and the theoretically calculated reflection spectra of the single-layer silica ARC and MgF$_2$. (Reprinted with permission from Moghal, J., et al., High-performance, single-layer antireflective optical coatings comprising mesoporous silica nanoparticles, *ACS App. Mater. Interfaces* 4, 2 (2012), 854–859. Copyright 2012 American Chemical Society.) (c) The schematic illustration of the double-layer broadband silica ARC. A reasonable RI gradient from air to the substrate was produced with ordered mesopores in the bottom layer and particle-packed pores in the top layer. (d) The transmittance spectra of the experimental and theoretical fitting double-layer silica ARCs and the quartz substrate, overlaid with the solar spectral irradiance at air mass (AM) 1.5. The prepared broadband coating showed consistency of the optical transmission of the double-layer broadband ARC with the solar spectrum. (e) The cross-sectional SEM image of the double-layer broadband silica ARC, from which the thickness of each layer was clearly observed. The broadband ARC was coated on a silicon wafer, and the cross-section of the coating was sprayed with Au nanoparticles prior to SEM imaging. (Reproduced from Sun, J., et al., A broadband antireflective coating based on a double-layer system containing mesoporous silica and nanoporous silica, *J. Mater. Chem. C,* 3 (2015), 7187–7194. By permission of The Royal Society of Chemistry.)

incident radiation. The reflection losses are reduced to only 5.9% by applying a three-layer graded-index ARC to Si (Figure 15.4c) [43]. A four-layer tailored- and low-RI ARC on an inverted metamorphic (IMM) triple-junction solar cell device is demonstrated (Figure 15.4d). By utilizing the oblique-angle e-beam deposition and physical vapor deposition (sputtering) methods, the four-layer ARC was fabricated on an IMM solar cell device (Figure 15.4e). By incorporating tailored- and low-RI materials into the ARC design
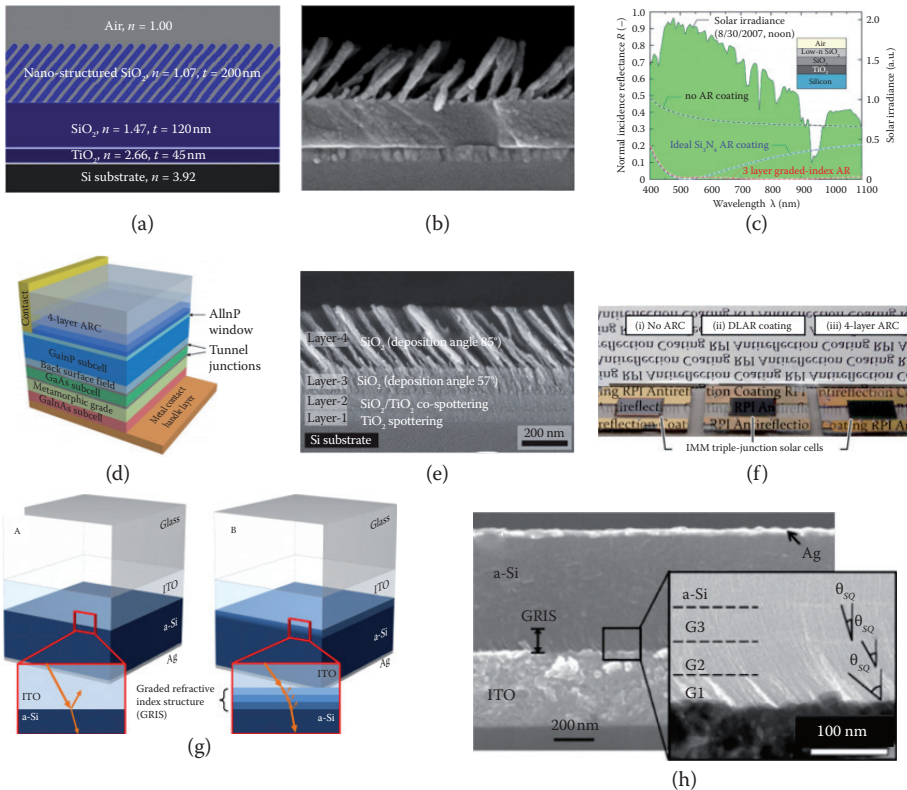
Figure 15.4 (a, b) Schematic and SEM image of three-layer graded-index AR coating; the refractive-index values are measured at 550 nm. (c) Solar spectrum and reflectance of silicon substrate with no AR coating, ideal Si3N4 AR coating, and three-layer graded-index AR coating. (Reprinted with permission from Chhajed, S., et al., Nanostructured multilayer graded-index antireflection coating for Si solar cells with broadband and omnidirectional characteristics, *Appl. Phys. Lett.,* 93 (2008), 251108. Copyright 2008 American Institute of Physics.) (d) Schematic layer sequence of an inverted metamorphic (IMM) triple-junction solar cell with four-layer AR coating. (e) SEM cross-sectional image of the four-layer AR coating deposited on a silicon substrate. (f) Photograph of three IMM solar cells with (i) no AR coating, (ii) double-layered AR coating, and (iii) four-layer AR coating. (Reproduced from Yan, X., et al.: Enhanced omnidirectional photovoltaic performance of solar cells using multiple-discrete-layer tailored- and low-refractive index anti-reflection coatings. *Adv. Funct. Mater.* 2013. 23. 583–590. Copyright Wiley-VCH Verlag GmbH & Co. KGaA. With permission.) (g) Schematic diagrams of typical superstrate-type thin-film solar cell structure (Sample A) and graded-index structure (Sample B). The magnified images in red squares express the light propagation through the interface between ITO and a-Si layer with and without the graded-index structure. (h) SEM image of the structure with the graded-index structure. The inset is a TEM image of the graded-index structure. (Reproduced from Jang, S.J., et al., Antireflective property of thin film a-Si solar cell structures with graded refractive index structure, *Opt. Express,* 19 (2011), 108–117. With permission of Optical Society of America.)

and fabrication, significant progress in terms of the optical efficiency was achieved in the implementation of quasi-continuously graded RI ARCs with so-called quintic or modified-quintic profiles. ARCs with these RI profiles are able to achieve improved broadband and omnidirectional AR characteristics in comparison to conventional double-layer ARCs (Figure 15.4f) [44].

The graded RI structure can also be applied to a thin-film amorphous-Si (a-Si) solar cell (Figure 15.4g and h). The graded RI structure fabricated using oblique angle deposition suppresses optical reflection in wide wavelength and incidence angle ranges compared to the conventional structure without graded index layers. Such graded index media are embedded inside the device structures, which are not available in conventional micro or nanostructures. The average reflectance of the thin-film a-Si solar cell structure with the graded RI structure is suppressed by 54% at normal incidence owing to effective RI matching between indium tin oxide and a-Si [45].

### 15.3.3 POROUS ARC

As mentioned in Chapter 2, subwavelength-scale porous materials could have AR properties. Usually, such porous materials are generated using chemical etching of a substrate. Among the fabrication methods of Si nanostructures, metal-assisted chemical etching has attracted increasing attention in recent years owing to simplicity and low operating costs [46,47]. A nanoscale porous structure is the typical morphology of Si etched using the metal-assisted chemical etching method. In a typical metal-assisted chemical etching procedure, a Si substrate partly covered by a noble metal is subjected to an etchant composed of HF and an oxidative agent. Typically, the Si beneath the noble metal is etched much faster than Si without noble metal coverage. As a result, the noble metal sinks into the Si substrate, generating pores in the Si substrate or, additionally, Si wires [47].

Such porous silicon structures show a prominent AR property. Porous Si fabricated by etching a polycrystalline Si substrate in a Ag particle–loaded Si substrate in a $H_2O_2$/HF solution revealed reduced reflectances in the wavelength range of 300–800 nm (Figure 15.5a and b) [48]. Wafer-scale silicon nano and microwires are also fabricated by using metal-assisted electroless etching for solar cell applications (Figure 15.5c–g). The optical reflectance spectra of the co-integrated wire samples are varied as a function of KOH etching in the wavelength range of 300–1000 nm (Figure 15.5h). The highest reflectance of the agglomerated nanowires (KOH 0 s) is not greater than ~2.5%, with an average reflectance of ~2.0% in the range of 300–1000 nm [49].

### 15.3.4 MOTH-EYE ARC

The biomimetic moth-eye structure can be understood easily in terms of a thin film, in which the RI changes gradually from the structure top to the bulk materials [50]. In case of a structured film with a gradient RI, we can regard the reflectance of the moth-eye surface as a resultant of an infinite series of reflections at each incremental change in the index [51]. To fabricate a high-performance artificial moth-eye structure, three structural features are generally required: the height and period of the arrays and the distance between the arrays. For the moth-eye surface, the period of the structures should be sufficiently small so that the array cannot be resolved by incident light. If this condition is fulfilled, we assume that at any depth, the effective RI is the mean of that of air and the bulk materials, weight in proportion to the volume of the materials. The condition that the moth-eye array should not be resolved by light is that the direction of the first diffracted order is over the horizon. For an ideal case of the moth-eye structure, it should show a tapered profile, the period should be as fine as possible, and the depth should be as great as possible to provide the widest bandwidth and almost omnidirectional antireflective properties [52].

Many techniques based on top-down lithography, such as electron-beam lithography [53,54], focused ion beam [55], interference lithography [56–58], and nanoimprint lithography [59], have been applied to fabricated AR structured surfaces. To avoid scattering from the optical interface, its structure dimension has to be smaller than the wavelength of the incident light [11,60]. For UV and visible light applications, the feature size should always be below 200 nm. In such a small size range, conventional top-down lithographic technologies (electron-beam etching and fast atom beam) require sophisticated equipment and are time-consuming and expensive for large-area fabrication for practical applications. To overcome the limitations of electron-beam etching, nanoimprint lithography is introduced to fabricate various functional polymer nanopillar arrays with a high throughput [61,62]. Moreover, by using such polymer arrays as masks, many functional material nanopillar arrays can be prepared by utilizing reactive ion etching (RIE).

Colloidal lithography is a low-cost and relatively high-throughput technique for patterning nanostructures [41]. The advantage of colloidal lithography in nanofabrication is that large-area self-assembly of colloids having well-ordered structures can be performed without expensive equipment [63,64]. Colloidal lithography is a simple, cost-effective, time-effective, and reproductive method to fabricate moth-eye structures on many materials [65–69]. Two-dimensional (2D) colloidal crystals are used as etch masks on a substrate [64,70]. Then, substrates are etched by implementing RIE [71]. In the process of RIE, the sphere masks can also be etched by reactive ions, and with an increase in the etching duration, the sphere masks were etched away gradually. Therefore, as the traverse diameter of a sphere was decreased, the etched area of an underlying substrate increased gradually, whereas the top diameter of the obtained structure was nearly the same as the traverse diameter of the sphere above, which led to the shape transformation of the
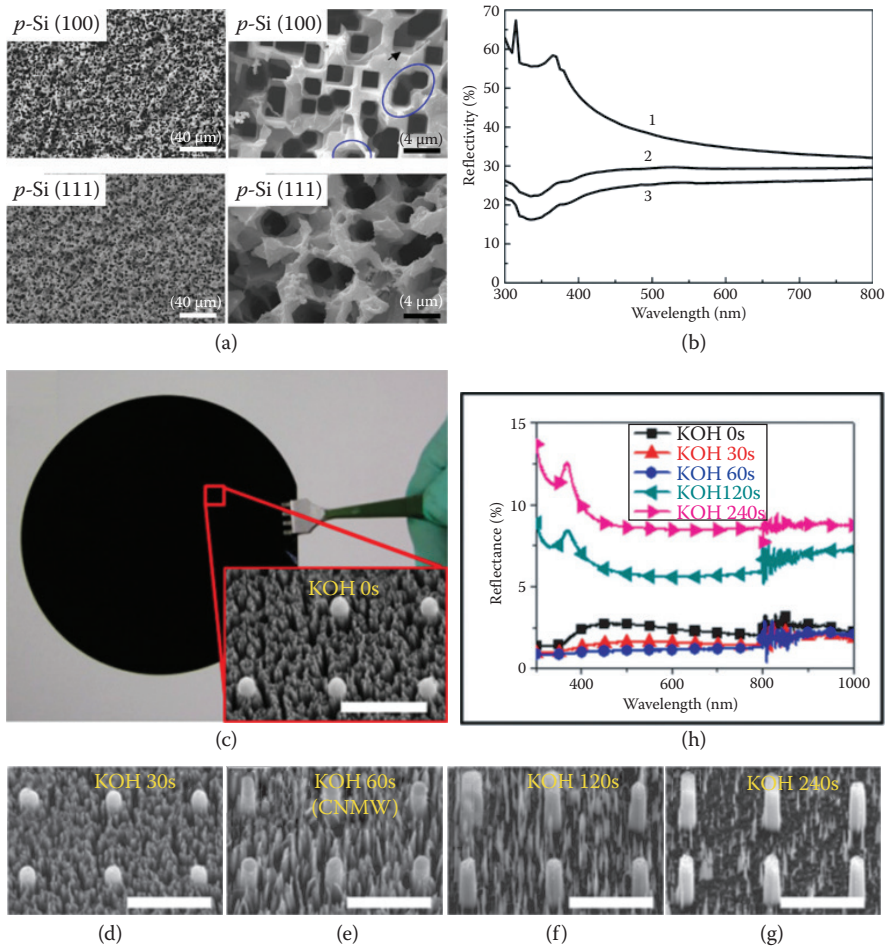
**Figure 15.5** (a) SEM images of p-Si wafers subjected to MacEtch in 1:1:1 (v:v:v) HF (49%):$H_2O_2$ (30%):ethanol solution for 12 h at 300 K by using catalytic Ag particles deposited on Si via silver-mirror reaction. The top macroporous layers were removed by dipping in NaOH (1%) for 15 min. The used wafers are p-Si (100) and p-Si (111). The images are displayed at different magnifications and orientations. (b) The reflectivity of the samples before and after MacEtch. Curves 1, 2, and 3 represent the unetched p-Si (100), etched p-Si (111), and etched p-Si (100) samples, respectively. (Reproduced with kind permission from Springer Science+Business Media: *J. Electron. Mater.*, Metal-assisted chemical etching using Tollen's reagent to deposit silver nanoparticle catalysts for fabrication of quasi-ordered silicon micro/nanostructures, 40, 2011, 2480–2485, Geng, et al.) (c) The photograph showing the wafer scale (4-inch) fabrication of a co-integrated, tapered nano and microwire (CNMW) structure. The effect of the KOH etching time after the formation of a CNMW structure is shown using 30°-tilted view SEM images: (c) 0, (d) 30, (e) 60, (f) 120, and (g) 240 s with the same scale bars of 10 μm. (h) The optical reflectance spectra of the CNMW samples as a function of the KOH etching time. (The source of the material Jung, J.-Y., et al., A waferscale Si wire solar cell using radial and bulk p–n junctions, *Nanotechnology*, 21, 445303, 2010 is acknowledged.)

obtained structure from cylinder to frustum of cone. When the sphere disappeared, the obtained textured profile started to change from the frustum of a cone to a cone because the top region of the etched substrate was nearer to the plasma, and thus it was etched more rapidly than narrow bottom areas between the frustum of the cones. Using colloidal lithography, subwavelength pyramidal and honeycomb structures are fabricated and optimized in solar cells. Subwavelength-scale monolayer and bilayer polystyrene spheres are combined using the one-step reactive ion etching process to fabricate optimized pyramid- and honeycomb shaped AR structures, respectively. A close-packed monolayer of 350 nm-diameter polystyrene spheres was coated on a silicon substrate using a dip coater (Figure 15.6a). The period of the pyramidal structure remained 350 nm, and the height was 480 nm (Figure 15.6b). Etched silicon has a height of 310 nm and a
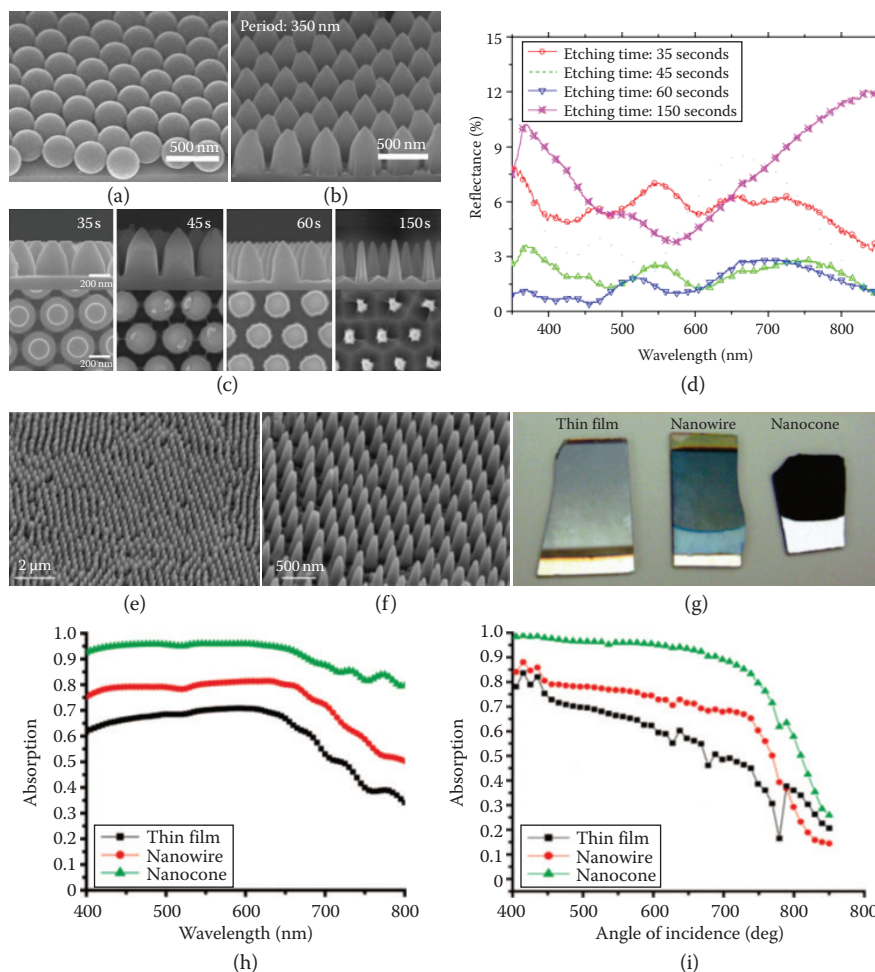
**Figure 15.6** (a) Close-packed monolayer of 350-nm-diameter polystyrene spheres coated on a silicon substrate. (b) The SEM image of pyramidal structures (period: 350 nm) transferred to silicon. (c) The top-view and cross-sectional images of the textured profiles obtained after etching for 30, 60, 100, and 150 s. (d) The measured reflectance spectra of the textured silicon samples prepared using various etching durations. (Reproduced from Chen, H.L., et al., Using colloidal lithography to fabricate and optimize sub-wavelength pyramidal and honeycomb structures in solar cells, *Opt. Express,* 15 (2007), 14793–14803. With permission of Optical Society of America.) (e) SEM images in a large area of a monolayer of a-Si:H nanocone arrays. (f) Zoom-in SEM images of a-Si:H nano-cone arrays. (g) Photographs of a-Si:H thin film (left), nanowire arrays (middle), and nanocone arrays (right). (h-i) Measured value of absorption on samples with a-Si:H thin film, nanowire arrays, and nanocone arrays as top layer over (h) a large range of wavelengths at normal incidence and (i) different angles of incidence (at wavelength λ = 488 nm). (Reprinted with permission from Zhu, J., et al., Optical absorption enhancement in amorphous silicon nanowire and nanocone arrays, *Nano Lett.,* 9 (2009), 279–282. Copyright 2009 American Chemical Society.)

small flat roof appeared when the etching was performed for 35 s. Upon increasing the etching duration, the top of etched silicon became sharper and the width narrower. The height of etched silicon increased to 480 nm (60 s) then decreased to 380 nm (150 s) (Figure 15.6c). The reflectance within the wavelength regime from 350 nm to 850 nm was less than 2.5% for the sample obtained at an etching duration of 60 s (Figure 15.6d) [68].

Nanocone arrays using a wafer-scale Langmuir–Blodgett assembly and etching technique are fabricated for enhanced broadband AR in solar cell applications (Figure 15.6e–f). The Langmuir–Blodgett method was used to assemble silica nanoparticles into a close-packed monolayer on top of an a-Si:H thin film. These silica nanoparticles were then used as an etch mask during a chlorine-based RIE process. It is believed that the conical shape is due to the gradual shrinkage of the size of the silica nanoparticle. After RIE, the silica

nanoparticles were so small that they were no longer observable on top of nanocones. The sample with nanocone arrays looks black, exhibiting enhanced absorption due to suppression of reflection from the front surface (Figure 15.6g). From Figure 15.6, it is obvious that, under identical conditions, the sample with nanocone arrays absorbed the most light, whereas the thin-film sample reflected the most light. The nano-cone arrays provided excellent impedance matching between a-Si:H and air through a gradual reduction in the effective RI away from the surface and, therefore, exhibited enhanced absorption due to superior AR properties over a large range of wavelengths and angles of incidence (Figure 15.6h–i) [72].

## 15.3.5 IDEAL GEOMETRY OF THE MOTH-EYE ARC

By the observation of corneal nipple arrays of various butterfly species and reflectance calculations of three different types of subwavelength structures (SWSs) using a thin-film multilayer model, Stavenga et al. showed that the parabola shape provides better AR properties than the cone and Gaussian-bell shapes [10]. In the EMT, the parabola shape yields a nearly linear RI gradient, which is efficient to reduce the surface reflection. To obtain SWSs with a conical profile, many fabrication methods, such as electron-beam/interfer-ence lithography [58,73–78], nanoimprint lithography [74,79,80], nanosphere or colloid formation [81–84], metal nanoparticles [85,86], and Langmuir–Blodgett assembly [72,87], have been proposed. However, it is difficult for these techniques to guarantee the formation of the parabola shape because the shape of the SWSs depends on complicated process control. However, the combination of interference lithography, thermal reflow, and subsequent pattern transfer is used to obtain the ideal shape of the moth-eye structure (Figure 15.7a). The fabricated SWSs consist of parabolic grating patterns, resulting in a linearly graded index profile. An increase in the process pressure improves the etch selectivity of PR, which leads to a taller height.
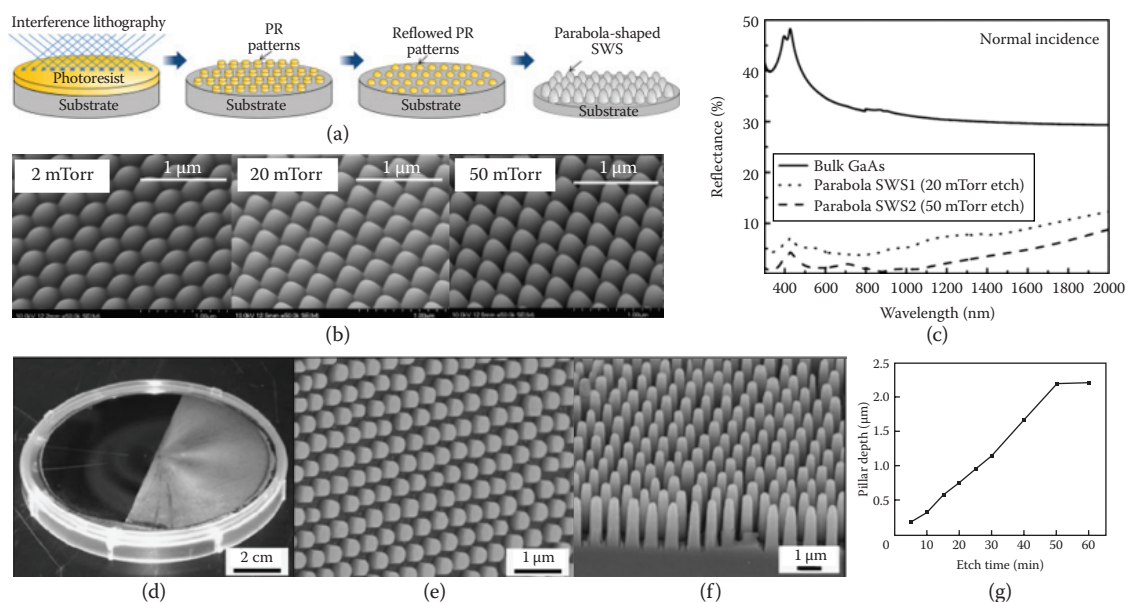


**Figure 15.7** (a) Schematic illustration of the fabrication procedure of the parabola-shaped SWSs on the GaAs substrate used in this experiment. The scale bar in the SEM images is 500 nm. (b) The SEM images of the parabola-shaped SWSs fabricated at process pressures of 2, 20, and 50 mTorr. (c) The measured reflectance as a function of the wavelength for the fabricated parabola-shaped SWSs on the GaAs substrate at process pressures of 20 mTorr and 50 mTorr. The measured reflectance of bulk GaAs is shown as a reference. Templated silicon pillar arrays by using a nonclose-packed colloidal monolayer. (Reproduced from Song, Y.M., et al.: Bioinspired parabola subwavelength structures for improved broadband antireflection. *Small*. 2010. 6. 984–7. Copyright Wiley-VCH Verlag GmbH & Co. KGaA. With permission.) (d) The photograph of a 4-inch silicon wafer with the right half cov-ered by subwavelength pillars and the left half unetched. The sample is illuminated by white light. (e) The silicon pillars after 10 min RIE. (f) The silicon pillars after 50 min RIE. (g) The pillar depth dependence on the RIE dura-tion. (Reproduced from Min, W.-L., et al.: Bioinspired self-cleaning antireflection coatings. *Adv. Mater.* 2008. 20. 3914–3918. Copyright Wiley-VCH Verlag GmbH & Co. KGaA. With permission.)

The etch selectivity is varied from 1 to 3 simply by increasing the process pressure from 2 to 50 mTorr. This means that the aspect ratio, that is, the height under the same period, can be controlled easily by adjusting the process pressure during the ICP etching procedure without the use of a complex gas mixture or additional process steps. The morphology of the etched surface through the lens-like PR mask is smooth, and these grating patterns are uniform (Figure 15.7b). Two SWS samples on the GaAs substrate suppress drastically the Fresnel reflection compared to that of the flat GaAs surface (Figure 15.7c) [56]. Based on a simple and scalable spin-coating technique that enables wafer-scale production of colloidal crystals with ncp structures, colloidal lithography is also used to obtain uniform moth-eye structures with a high aspect ratio. Broadband silicon moth-eye structures have been fabricated by using a 2D ncp colloidal crystal as the etching mask during an $SF_6$ RIE process (Figure 15.7d–g). The nonwetting properties are also obtained to ultimately realize self-cleaning broadband ARCs on silicon substrates [88].

## 15.3.6 LARGE-SCALE FABRICATION OF ARCs

For high-performance broadband antireflective properties of the moth-eye structure over large areas, high-aspect ratio silicon random nanotip arrays are fabricated by using high-density electron cyclotron resonance plasma etching (Figure 15.8a–c). The geometric features of the silicon nanotip arrays were characterized by the apex diameter in the range of 3–5 nm, a base diameter of 200 nm, and lengths from 1 to 16 μm. Such AR structured surfaces can suppress light reflection in the wavelength range from UV, through the visible part of the spectrum, to the terahertz region. Reflection is suppressed in a wide range of the incidence angles and for both s- and p-polarized light. Excellent antireflective properties of such an antireflective structure are close to those of ideal antireflective surfaces (Figure 15.8d–g) [89].
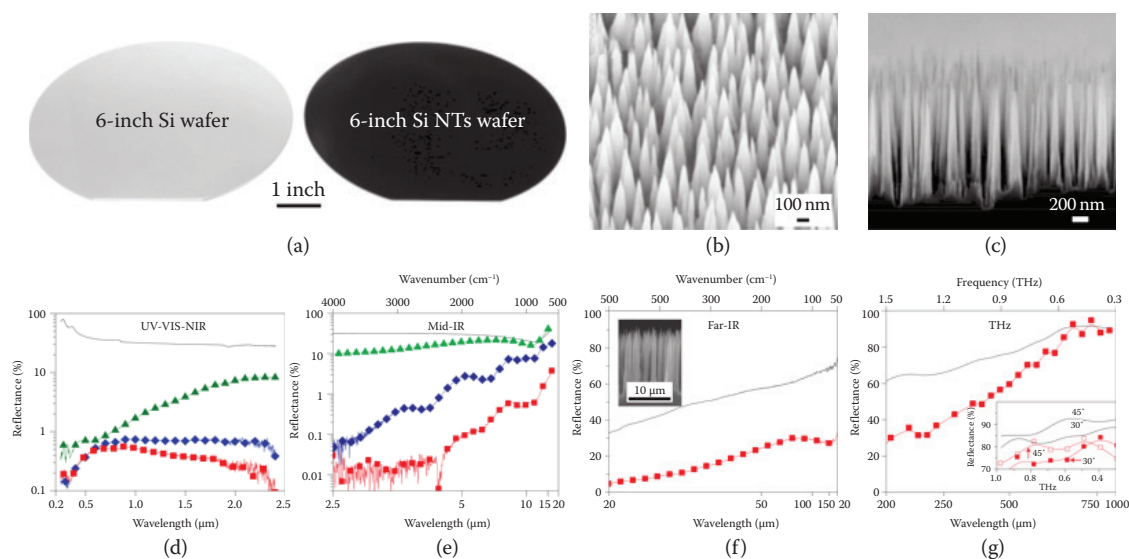


Figure 15.8 (a) Photographic images showing the 6 inch polished silicon wafer (left) and the wafer coated with Si nanotip structures (right). The SEM images showing the tilted top view (b) and the cross-sectional view (c) of Si nanotip structures with a length of 1,600 nm. (d) The hemispherical reflectance (using an integrating sphere) as a function of the wavelength for a planar Si wafer (solid line, black) and Si nanotip structures (symbols) for L = 1.6 (green), 5.5 (blue), and 16 μm (red) at the UV, visible, and near-infrared wavelengths. (e) The specular reflectance (without an integrating sphere) as a function of the wavelength in the mid-infrared region for an incidence angle of 30°. (f–g) Comparison of the specular reflectance as a function of the wavelength for a planar silicon wafer (solid line, black) and Si nanotip structures with L = 16 μm (red) in the far-infrared (f) and terahertz (g) regions for an incidence angle of 30°. The inset in (f) shows the cross-sectional SEM image of the Si nanotip structures with L = 16 μm. The inset in (g) compares the reflectance in planar silicon (solid line, black) and Si nanotip structures (symbols, red) with unpolarized light and an incidence angle of 30° (filled squares) and 45° (open squares). The solid red lines in the inset of (f) are guides to the eye. (Reprinted by permission from Macmillan Publishers Ltd: *Nature Nanotechnology* [89], copyright © 2007.)

Functional materials

### 15.3.7 COMPOUND-EYE ARC—HIERARCHICAL MICRO AND NANOSTRUCTURES

An antireflective compound-eye surface structure was generated by applying the moth-eye structure to another structure. By employing KOH etching and silver catalytic etching, pyramidal hierarchical structures were generated on the crystalline silicon wafer (Figure 15.9a–c). The hierarchical structures exhibited strong AR and superhydrophobic properties after fluorination (Figure 15.9d). Furthermore, a flexible superhydrophobic substrate was fabricated by transferring a hierarchical Si structure to NOA 63 film using UV-assisted imprint lithography. This method is of potential application in optical, optoelectronic, and wettability control devices [90].

The details of the AR technologies discussed in this chapter, including AR mechanisms, AR materials, fabrication methods, AR structure, and final reflection, are summarized in Table 15.1.
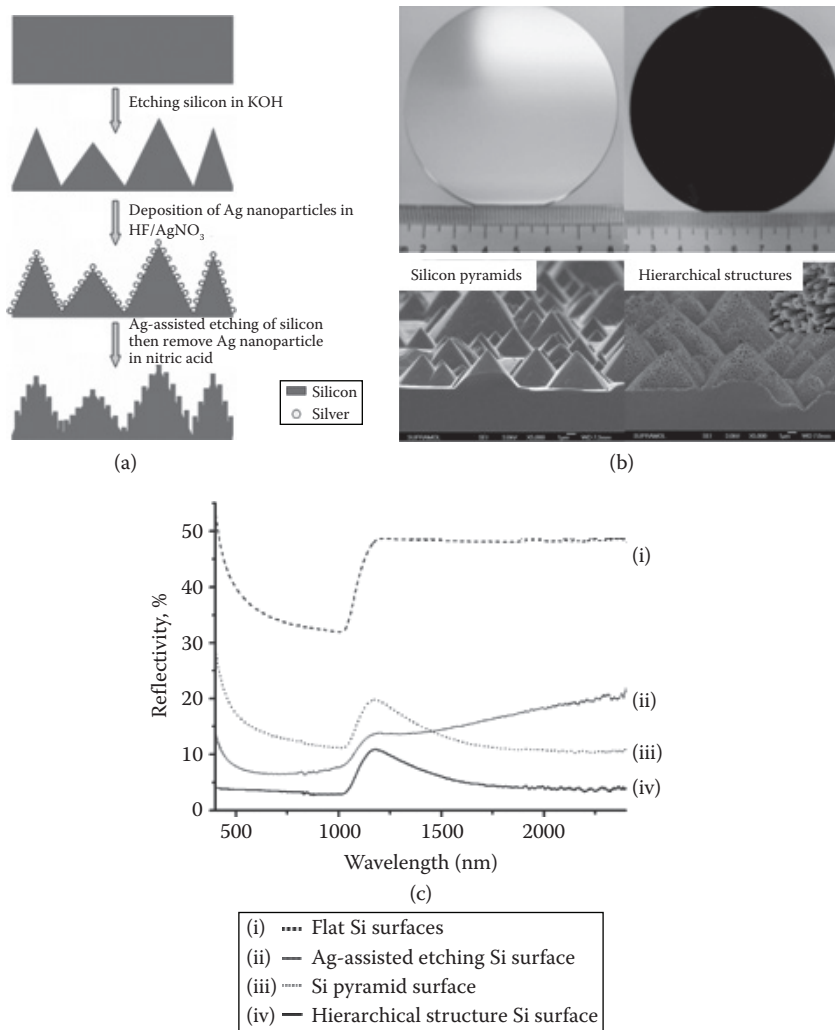


Figure 15.9 (a) Fabrication procedure for creating hierarchical structures on the silicon surface. (b) The photographs of the polished silicon wafer (left) and the hierarchically structured silicon wafer (right). (c) The cross-sectional SEM photographs of silicon pyramids created using KOH etching and hierarchical structures generated by utilizing Ag-assisted etching. The inset is the magnified SEM image. (d) The hemispherical reflectance spectra of flat silicon (i), nanohole textured silicon surface (ii), pyramid textured silicon surface (iii), and hierarchically structured silicon (iv). (Reprinted with permission from Qi, D., et al., Simple approach to wafer-scale self-cleaning antireflective silicon surfaces, *Langmuir,* 25, 14 (2009), 7769–7772. Copyright 2009 American Chemical Society.)

Table 15.1 **Summary of technical details of the AR technologies discussed in this chapter**

| TYPE | FABRICATION METHODS | MATERIALS | REFLECTION, % | REFERENCE |
|---|---|---|---|---|
| Quarter-wavelength | Seeding and growth method | ZnO nanostructures | ~6.6 | [91] |
| | Convective assembly | $SiO_2$ | ~11 | [92] |
| | Spin coating | $TiO_2$ | ~8 | [93] |
| Multilayer | Remote PECVD | Porous $SiO_2$/SiN | <1 | [94] |
| | Electron cyclotron resonance PECVD | $SiO_2$/$TiO_2$ | <0.5 | [95] |
| | PECVD | SiN | <3 | [96,97] |
| | Immersion in carbonate-based solutions followed by stain etching | Carbonate-based solutions, $HNO_3$/HF and $SiN_x$ | 3.16 | [98] |
| Graded index | Oblique-angle deposition | $TiO_2$/$SiO_2$/ nanostructured $SiO_2$ | 5.9 | [43] |
| | Electron beam lithography followed by SF6 etching | EB-positive resist | 0.5 | [54] |
| | Spin coating, etching | $SiO_2$ | <2 | [88,99] |
| | Reactive ion etching | – | <3 | [100] |
| Porous ARC | Electrochemical etching | Ethanol-based solution of 33.3 wt% HF | 8.93 | [101] |
| | Interference lithography and then metal-assisted chemical etching | Si photonic crystals | ~3 | [102] |
| | Electochemical etching, HF:ethanol, (1:4 ratio) | HF:ethanol, (1:4 ratio) | ~1 | [103] |
| | Spin coating, RIE, templating | $SiO_2$ and polymer posts, gold nanoholes | <0.5 | [104] |
| Moth eye | Spin coating and then anisotropic wet etching | $SiO_2$ | ~2 | [82] |
| | Nanoimprint technique | UV-sensitive resist | ~1 | [105] |
| | Microreactor-assisted nanomaterial deposition | Solution-processed Ag nanoparticles, ZnO | 3.4 | [106] |
| | Reactive ion etching | Polystyrene nanobeads | ~3.8 | [107] |
| | UV-nanoimprint lithography | Anodized aluminum oxide | 4 | [108] |
| | Spin coating, RIE | $SiO_2$ | <2.5 | [83] |

## 15.4 OPTICAL DEVICE APPLICATIONS

Thin-film crystalline silicon (c-Si) solar cells are one of the promising candidates for low-cost photovoltaic applications because of commercially compatible mass-production processes. However, a relatively thin absorption region tends to degrade the cell efficiency, which is the main drawback of thin-film solar cells [109]. To improve light absorption in thin-film solar cells, the Fresnel reflection at the air/silicon interface in the range of the entire solar spectrum should be minimized. For silicon solar cell applications,

broadband AR is needed to cover the whole absorption range of silicon in the solar spectrum. Moreover, to achieve a high absorption efficiency for the entire day, the angle-independent AR property is required [20]. Conventional thin-film ARCs exhibit reflection reduced by their interference principle; however, this can only work in a limited wavelength range. Although multilayer ARC is commonly used for broadband AR, it has problems related to material selection, thermal mismatch, and instability of thin-film stacks [4]. As an alternate to thin-film coatings, submicrometer grating (SMG) structures with a tapered feature, originally inspired by the excellent antireflective capability of the corneal of night-active insects, have been focused on as a more practical method for ultra broadband and omnidirectional ARs (Figure 15.10a). In comparison to single-layer and double-layer ARCs, the calculated reflectance of SMG structures on the top surface of c-Si has broader AR regions (Figure 15.10b). Tapered structures with a taller height and a shorter period are desirable for broadband AR properties; however, a taller structure requires complex process steps, which increase the fabrication cost. Therefore, the optimum geometry with an appropriate height and period is needed in practical solar cell applications. SMG structures with a period of 400 nm and a height of 400 nm exhibit a higher cell efficiency in a reasonable process range (Figure 15.10c). The cell efficiency of c-Si solar cells with a flat surface drops rapidly as the incidence angle increases because of the increased reflection loss. However, in SMG-integrated solar cells, the cell efficiency is stable at an incidence angle greater than 60°, and it is degraded by only 8.3% at 70° compared to that at 0° (Figure 15.10d) [20].
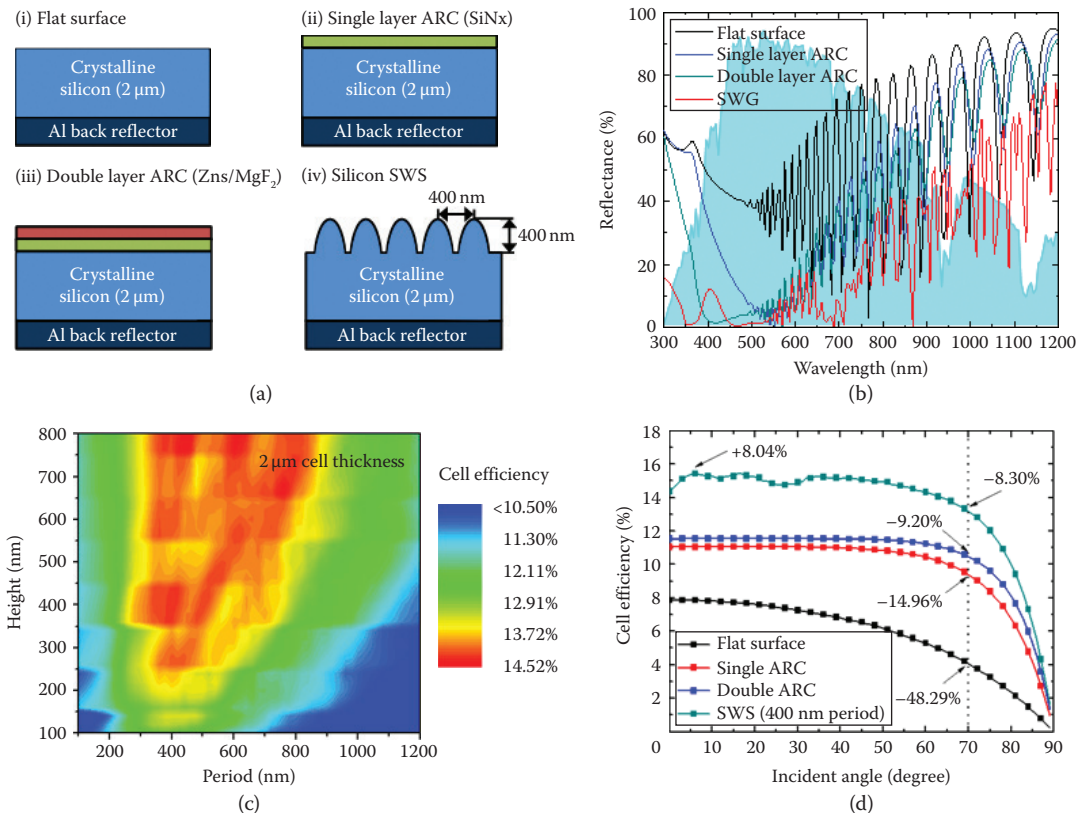


**Figure 15.10** (a) Thin-film c-Si solar cells with four different surface structures: (i) flat surface, (ii) single-layer ARC, (iii) double-layer ARC, and (iv) antireflective SWSs. (b) The calculated reflectance spectra of thin-film c-Si solar cells with an Al metallic back reflector for four different surface structures. AM 1.5 solar spectrum is also shown as a reference. (c) The contour map for the cell efficiency of the SWS integrated thin-film c-Si solar cells as a function of the cone period and height. (d) The cell efficiencies of the 2-μm-thick c-Si solar cells with four different surface structures as a function of incidence angle. The period and height of the SWSs are 400 nm. (Reproduced form Song, Y.M., et al., Antireflective submicrometer gratings on thin-film silicon solar cells for light-absorption enhancement, *Opt. Lett.,* 35, 3 (2010), 276–278. With permission of Optical Society of America.)

The device exhibits a higher performance at a slightly tilted incidence angle compared to the normal incidence angle. This efficiency enhancement is attributed to the extended optical path length [110].

Silicon nanostructure arrays have the potential to increase the power conversion efficiency of photovoltaic devices. Nevertheless, so far, photovoltaic cells based on nanostructured silicon exhibit lower power conversion efficiencies than conventional cells owing to enhanced photocarrier recombination associated with the nanostructures [111]. Increased photocarrier recombination at the dramatically increased surface area of nanostructured silicon decreases the cell efficiency by reducing the device short-circuit current $J_{sc}$ and open-circuit voltage $V_{oc}$. For example, in antireflective nanostructured silicon solar cells made by gold-nanoparticle catalyzed etching, increased recombination was observed, and it dramatically reduced the collection of photocarriers generated by blue and green (i.e., 350–600 nm) photons [112]. However, it was only possible to model the measured quantum efficiency of these nanostructured cells by including a dead layer extending ~500 nm beneath the front surface, in which the minority carrier lifetime was extremely low. This dead layer was roughly as thick as the nanoporous layer itself, and modeling with increased planar surface recombination alone could not be performed. It has recently been reported that the blue quantum efficiency could be increased by decreasing the nanopore depth, but this inevitably compromised the beneficial effects of the nanostructure for photon management [111,113].

Small cone-like subwavelength structures for solar cells were fabricated uniformly on the Si surface, although the periodicity was not perfect (Figure 15.11a). The period and height for the SWS were around 100 and 300 nm, respectively. Test solar cells were fabricated to demonstrate the wideangle AR effect of the SWS in solar cells. A Si SWS with a high aspect ratio was fabricated on p-type Czochralski-grown (CZ) Si wafers by dry etching using anodic porous alumina masks. After the formation of the SWS, phosphorus diffusion was carried out using a standard quartz tube furnace with POCl$_3$ at 850°C to fabricate a p–n junction. A Ag-based front grid and Al rear contact were formed by vacuum evaporation and successive firing. The finger grid pattern on the front side with a covered area of about 11% was fabricated by photolithography. The spectral reflectivity of the SWS measured using diffuse reflection optics shows a very low reflectivity over a wide range of wavelengths (Figure 15.11b). The SWS cell clearly showed higher short-circuit current density, $J_{sc}$, and slightly higher open-circuit voltage, $V_{oc}$, than those of the flat cell. These improvements are attributable to the reduction of surface reflection loss by the SWS. However, the obtained $J_{sc}$ for the SWS cell was lower than expected from its very low reflectivity (R ~ 1%). This is mainly due to the carrier recombination at the surface and highly doped emitter region. The SWS cell shows lower internal quantum efficiency (IQE) at shorter wavelengths than the flat cell, which causes the relatively low $J_{sc}$ (Figure 15.11c) [114]. A sub-100 nm surface-oxidized silicon nanocone forest structure is created and integrated onto the existing texturization microstructures on a photovoltaic device surface by a one-step high-throughput plasma-enhanced texturization method (Figure 15.11d). The surface of silicon can be nanotexturized with the simultaneous plasma-enhanced reactive ion etching and synthesis (SPERISE) process carried out in a plasma etcher with O$_2$ and HBr gas mixture. The bromine ion plays the role of etching and texturizing while the oxygen ion plays the role of nanosynthesis and oxidizing passivation. According to the EMT, the gradually varying RI of the cone forest structure can dramatically reduce the reflection and thus make the silicon surface black. The nanocone forest structure dramatically reduces the optical reflection by 70.25% (Figure 15.11e). The I–V characteristics of the solar cell measured under one sun indicates that our nanotexturization method can improve the open-circuit voltage by a little, short-circuit current by 7.09%, fill factor by 7.0%, and conversion efficiency by 14.66%. The quantum efficiency is also increased by 14.31% (Figure 15.11f). Although the reflectance of the solar cell surface is suppressed by the nanotexturization in the whole wavelength range from UV to IR, the EQE only improved in most of the visible and near-IR region. In terms of the conversion efficiency, there must be some competition between the increase by absorption enhancement and the decrease by surface recombination. That is, the absorption enhancement dominates in the visible and near-IR region, whereas the surface recombination dominates in other regions [115].

Despite great efforts to directly produce antireflective nanostructures on Si solar cells in various ways, several problems are still difficult to be considered. For so-called superstrate-type thin-film solar cells, where active cells are deposited onto transparent glass covered by a transparent conducting oxide, the
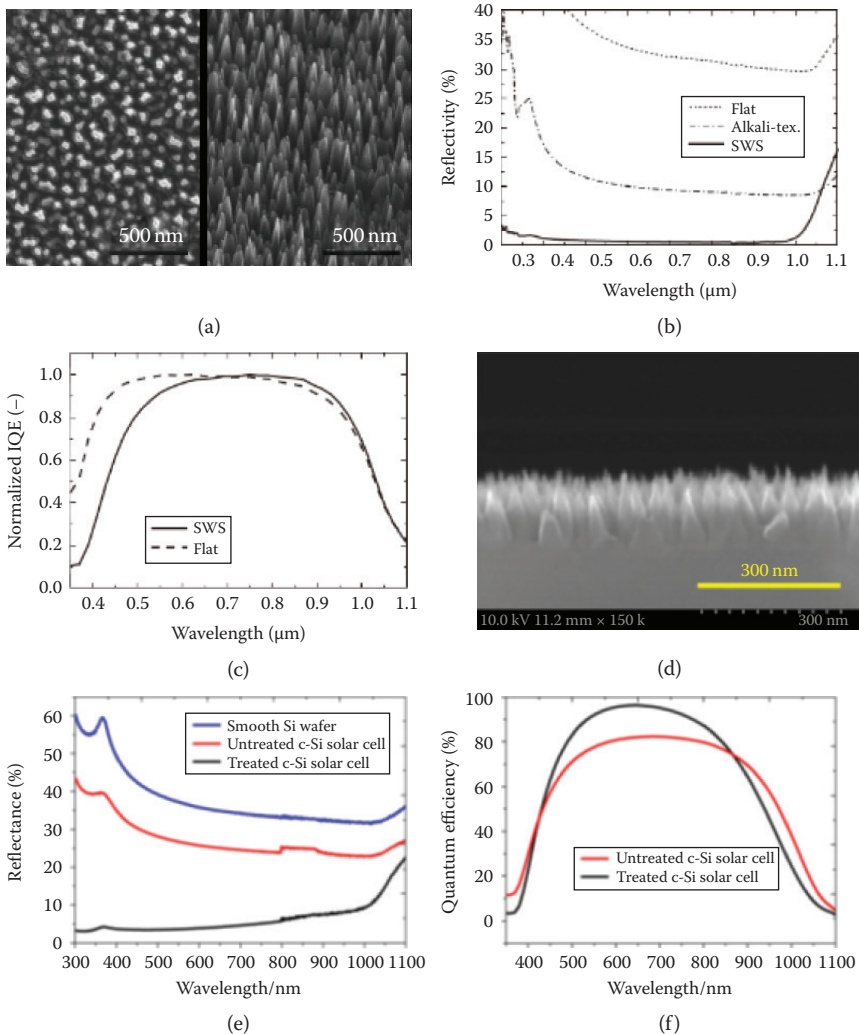
**Figure 15.11** (a) SEM images of the fabricated subwavelength structure (SWS) on Si surface (left: top view, right: oblique view). (b) Measured reflectivity of the fabricated Si SWS at normal incidence. (c) Normalized IQE of the test solar cells with SWS and flat surface. (Reprinted from Sai, H., et al., Wide-angle antireflection effect of subwavelength structures for solar cells, *Jpn. J. Appl. Phys.* 46 (2007): 3333–6. Copyright 2007 The Japan Society of Applied Physics. With permission.) (d) Cross-sectional SEM image of sub-100 nm surface-oxidized silicon nanocone forest structure. (e) Diffusive reflection spectra of smooth Si wafer (blue), untreated c-Si solar cell (red), and nanotexturized c-Si solar cell (black). (f) EQE spectra of commercial solar cell before (red curve) and after (black curve) nanotexturization treatment. (Reproduced from Xu, Z., et al., Lithography-free sub-100 nm nanocone array antireflection layer for low-cost silicon solar cell, *Appl. Opt.,* 51 (2012): 4430–4435. With permission of Optical Society of America.)

reflection at the interface between air and glass should be minimized. An alternative way to apply antireflective nanostructures onto a thin-film solar cell is the fabrication of disordered submicron structures (d-SMSs) on the top glass substrate of superstrate-type thin-film hydrogenated amorphous silicon (a-Si:H) solar cells to improve the light absorption (Figure 15.12a). The d-SMSs with a tapered shape were fabricated on the back side of an $SnO_2$:F covered glass substrate by using plasma etching of thermally dewetted silver nanoparticles without any lithography process (Figure 15.12b). The glass substrates with the d-SMSs showed a very low reflectance compared to that of the glass substrates with the flat surface in a wide specular and angular range (Figure 15.12c). Thin-film a-Si:H solar cells were prepared on the opposite side of the d-SMS integrated glass substrates, and the devices exhibited an increased short-circuit current density ($J_{sc}$)
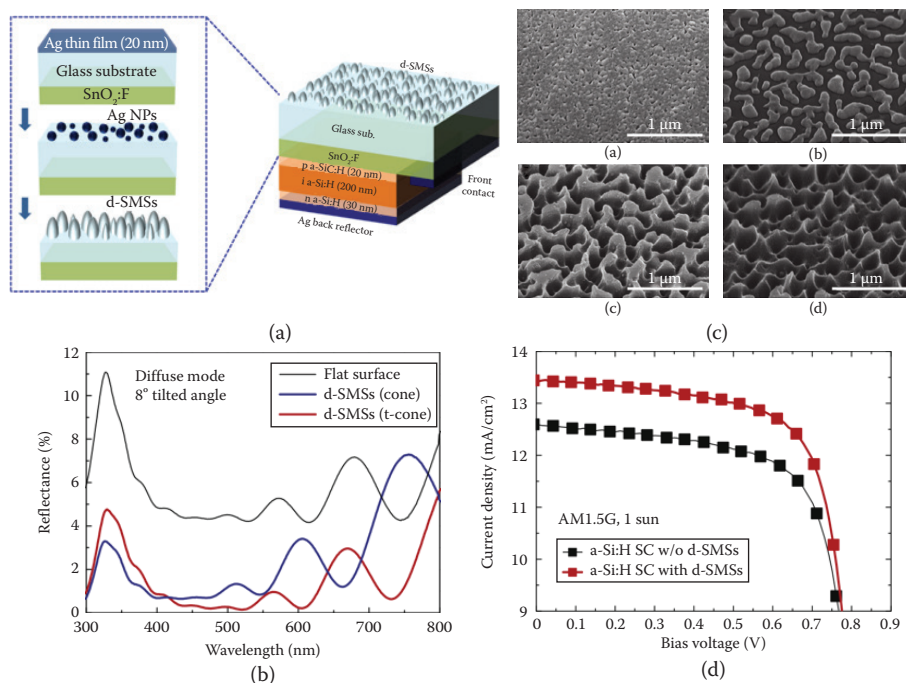
**Figure 15.12** (a) Schematic illustration of thin-film amorphous silicon (a-Si) solar cells with d-SMSs for broadband AR. The inset on the left shows the fabrication procedure of the d-SMSs by using thermally dewetted silver nanoparticles. (b) The SEM images of (i) as a Ag thin film deposited on a glass substrate, (ii) Ag nanoparticles thermally dewetted at 500°C for 1 min. The fabricated d-SMSs using dry etching of Ag nanoparticles in ICP-RIE for (iii) 7 min and (iv) 9 min, respectively. (c) The measured reflectances of three different types of glass substrates (flat surface, cone shaped d-SMSs, and truncated cone-shaped d-SMSs) in the diffuse mode. (d) The J–V characteristics of thin-film a-Si:H solar cells with and without d-SMSs. (Reprinted from *Solar Energy Mater. Solar Cells*, 101, Song, Y.M., et al., Disordered submicron structures integrated on glass substrate for broadband absorption enhancement of thin-film solar cells, 73–78, Copyright 2012, with permission from Elsevier.)

by 6.84% compared to the reference cells with the flat surface without detrimental changes in the open-circuit voltages ($V_{oc}$) and the fill factor (Figure 15.12d) [116].

Besides silicon materials, antireflective nanostructures composed of many other materials were explored as ARCs, in spite of relatively less reports compared to those of silicon nanostructures. Antireflective nanostructures can be applied to various optoelectronic devices with AR surfaces constructed by nonsilicon antireflective nanostructures, mainly including group III–V compounds, and polymers. Group III–V semiconductors are widely used in optoelectronics, such as solar cells, LEDs, and lasers, because of their high carrier mobility and direct energy gaps. However, there are some challenges in the fabrication of broadband ARCs of most group III–V semiconductors, owing to their bandwidth disparity. Nanostructure arrays of group III–V materials with a gradient RI directly grown on the same substrates may be able to address the problems. Nanostructure arrays of group III–V semiconductors were usually fabricated through the vapor deposition growth or RIE methods, rather than solution methods owing to their intrinsic physicochemical properties. Antireflective polymer films were investigated intensively because of their advantageous characteristics compared to inorganic materials, such as easily controllable morphology and porosity, adherence to a flexible substrate, and ease of large-area processing. For preparing polymer ARCs based on nanostructure arrays, the most widely used technique is template imprinting [17]. Parabola-shaped ARNSs were fabricated using simple process steps based on the combination of laser-interference lithography, thermal reflow, and subsequent pattern transfer [56]. The use of the additional thermal-reflow process makes lens-shaped photoresist patterns, which enable pattern transfer to realize the parabola shape. Parabola-shaped ARNSs on a GaAs substrate fabricated by the lens-like shape-transfer method resulted in a linearly graded index profile. The morphology of the etched surface is smooth, and the grating patterns are uniform.
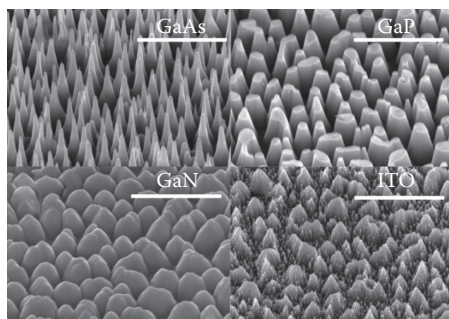
**Figure 15.13** SEM images of ARNSs on GaAs, gallium phosphide, gallium nitride, and indium tin oxide substrates fabricated using dry etching of thermally dewetted silver nanoparticles. Scale bars: μm. (Reproduced from Song, Y.M., and Lee, Y.T., Antireflective nanostructures for high-efficiency optical devices, *SPIE Newsroom*, November 30, 2010. With permission of SPIE.)

The fabricated sample shows AR properties in a broader wavelength range than that of the flat surface or even conventional cone-shaped ARNSs. Another approach for ARNSs is the overall dry-etching process using thermally dewetted silver nanoparticles. In this method, the thermal dewetting process of thin metal films deposited by implementing electron-beam evaporation provides nanoscale etch-mask patterns without lithography, enabling cost-effective fabrication. Moreover, the average nanoparticle size and separation can be controlled by the film thickness at a given annealing temperature. Because the fabrication process is not limited to certain materials, ARNSs can be fabricated on various substrates (Figure 15.13) [117].

## 15.5 SUMMARY

The principle of AR layers/structures was discovered a few decades ago, and a number of manufacturing methods have been proposed for various materials, including silicon, germanium, III–V compound semiconductors, and transparent glasses/polymers. Nowadays, a promising application field of AR structures concerns optoelectronic devices/systems. In this review, we discussed several ARCs (i.e., single- or double-layer ARCs and gradient-index ARCs) and AR structures (i.e., tapered and nontapered porous structures and moth-eye structures). We also showed various fabrication methods of the above-mentioned layers/structures. In addition, optoelectronic device applications and design guidelines of ARCs for specific devices were discussed. We believe that our review will contribute to giving insights not only in developing simpler fabrication methods of ARCs on silicon or other semiconductor/dielectric materials but also in clear understanding of the reflection behavior of optoelectronic devices and the optimal geometry of ARCs.

## REFERENCES

1. Karen Forberich, Gilles Dennler, Markus C. Scharber, Kurt Hingerl, Thomas Fromherz, and Christoph J. Brabec, Performance Improvement of Organic Solar Cells with Moth Eye Anti-Reflection Coating, *Thin Solid Films* 516, 20 (2008): 7167–70, doi: 10.1016/j.tsf.2007.12.088.
2. Jia Zhu, Ching-Mei Hsu, Zongfu Yu, Shanhui Fan, and Yi Cui, Nanodome Solar Cells with Efficient Light Management and Self-Cleaning, *Nano Lett.* 10, 6 (2010): 1979–84, doi: 10.1021/nl9034237.
3. Jeri'Ann Hiller, Jonas D. Mendelsohn, and Michael F. Rubner, Reversibly Erasable Nanoporous Anti-Reflection Coatings from Polyelectrolyte Multilayers, *Nat. Mater.* 1 (2002): 59–63, doi: 10.1038/nmat719.
4. Philippe Lalanne and G. Michael Morris, Design, Fabrication, and Characterization of Subwavelength Periodic Structures for Semiconductor Antireflection Coating in the Visible Domain, *Proc. SPIE* 2776 (1996): 300–8, doi: 10.1117/12.246835.
5. Hyun Myung Kim, Sang Hyeok Kim, Gil Ju Lee, Kyujung Kim, and Young Min Song, Parametric Studies on Artificial Morpho Butterfly Wing Scales for Optical Device Applications, *J. Nanomater.* 2015, 451834 (2015): 7, doi:10.1155/2015/451834.
6. Rick C. Schroden, Mohammed Al-Daous, Christopher F. Blanford, and Andreas Stein, Optical Properties of Inverse Opal Photonic Crystals, *Chem. Mater.* 14, 8 (2002): 3305–15, doi: 10.1021/cm020100z.

7. Inhwa Jung, Jianliang Xiao, Viktor Malyarchuk, Chaofeng Lu, Ming Li, Zhuangjian Liu, and Jongseung Yoon, Dynamically Tunable Hemispherical Electronic Eye Camera System with Adjustable Zoom Capability, *Proc. Natl. Acad. Sci. U S A.* 108, 5 (2011): 1788–93, doi: 10.1073/pnas.1015440108.

8. C. G. Bernhard and William H. Miller, A Corneal Nipple Pattern in Insect Compound Eyes, *Acta Physiol. Scand.* 56 (1962): 385–6, doi: 10.1111/j.1748-1716.1962.tb02515.x.

9. Doo-Hyun Ko, John R. Tumbleston, Kevin J. Henderson, Larken E. Euliss, Joseph M. DeSimone, Rene Lopez, and Edward T. Samulski, Biomimetic Microlens Array with Antireflective "Moth-Eye" Surface, *Soft Matter* 7 (2011): 6404, doi: 10.1039/c1sm05302g.

10. Doekele Stavenga, S. Foletti, G. Palasantzas, and Kentaro Arikawa, Light on the Moth-Eye Corneal Nipple Array of Butterflies, *Proc. R. Soc. B* 273 (2006): 661–7, doi: 10.1098/rspb.2005.3369.

11. S. J. Wilson and M. C. Hutley, The Optical Properties of 'Mote Eye' Antireflection Surfaces, *Optica Acta* 29, 7 (1982): 993–1009, doi: 10.1080/713821334.

12. G. Palasantzas, J. T. M. de Hosson, K. F. L. Michielsenand, and D. O. Stavenga, Optical Properties and Wettability of Nanostructured Biomaterials: Moth-Eyes, Lotus Leaves, and Insect Wings, in *Handbook of Nanostructured Biomaterials and Their Applications in Biotechnology, Vol. 1: Biomaterials*, ed. Hari Singh Nalwa (California: American Scientific Publishers, 2005), 273–301.

13. Akihiro Yoshida, Mayumi Motoyama, Akinori Kosaku, and Kiyoshi Miyamoto, Antireflective Nanoprotuberance Array in the Transparent Wing of a Hawkmoth, *Cephonodes Hylas, Zool. Sci.* 14 (1997): 737–41, doi: 10.2108/zsj.14.737.

14. Taolei Sun, Lin Feng, Xuefeng Gao, and Lei Jiang, Bioinspired Surfaces with Special Wettability, *Acc. Chem. Res.* 38, 8 (2005): 644–52, doi: 10.1021/ar040224c.

15. Hongbo Xu, Nan Lu, Gang Shi, Dianpeng Qi, Bingjie Yang, Haibo Li, Weiqing Xu, and Lifeng Chi, Biomimetic Antireflective Hierarchical Arrays, *Langmuir* 27, 8 (2011): 4963–7, doi: 10.1021/la1040739.

16. Surojit Chattopadhyay, Yi-Fan Huang, Y. J. Jen, Abhijit Ganguly, K. H. Chen, and L. C. Chen, Anti-Reflecting and Photonic Nanostructures, *Materials Science and Engineering R* 69 (2010): 1–35, doi: 10.1016/j.mser.2010.04.001.

17. Jinguang Cai and Limin Qi, Recent Advances in Antireflective Surfaces Based on Nanostructure Arrays, *Mater. Horiz.* 2 (2015): 37–53, doi: 10.1039/C4MH00140K.

18. Hemant Kumar Raut, V. Anand Ganesh, A. Sreekumaran Nair, and Seeram Ramakrishna, Anti-Reflective Coatings: A Critical, in-Depth Review, *Energ. Environ. Sci.* 4 (2011): 3779–804, doi: 10.1039/c1ee01297e.

19. Eugene Hecht, *Optics*, 4th Edition (San Francisco, CA: Addison-Wesley, 2002), 3.

20. Young Min Song, Jae Su Yu, and Yong Tak Lee, Antireflective Submicrometer Gratings on Thin-Film Silicon Solar Cells for Light-Absorption Enhancement, *Opt. Lett.* 35, 3 (2010): 276–8, doi: 10.1364/OL.35.000276.

21. Won Il Nam, Young Jin Yoo, and Young Min Song, Geometrical Shape Design of Nanophotonic Surfaces for Thin Film Solar Cells, *Opt. Express* 24, 14 (2016): A1033, doi: 10.1364/OE.24.0A1033.

22. Young Min Song, Hee Ju Choi, Jae Su Yu, and Yong Tak Lee, Design of Highly Transparent Glasses with Broadband Antireflective Subwavelength Structures, *Opt. Express* 18, 12 (2010): 73–8, doi: 10.1364/OE.18.013063.

23. Young Jin Yoo, Ki Soo Chang, Suck Won Hong, and Young Min Song. Design of ZnS Antireflective Microstructures for Mid- and Far-Infrared Applications, *Opt. Quant. Electron.* 47 (2015): 1503–8, doi: 10.1007/s11082-015-0143-0.

24. J.-Q. Xi, Martin F. Schubert, Jong Kyu Kim, Ef Schubert, Minfeng Chen, S. H. Lin, Wen Liu, and Joseph A. Smart, Optical Thin-Film Materials with Low Refractive Index for Broadband Elimination of Fresnel Reflection, *Nature Photonics* 1 (2007): 176–9, doi: 10.1038/nphoton.2007.26.

25. J. C. Maxwell Garnett, Colours in Metal Glasses, in Metallic Films, and in Metallic Solutions. II, *Phil. Trans. R. Soc. Lond. A* 205 (1906): 237–88, doi: 10.1098/rsta.1906.0007.

26. J. C. Maxwell Garnett, Colours in Metal Glasses, in Metallic Films, and in Metallic Solutions. II, *Phil. Trans. R. Soc. Lond. A* 203 (1904): 385–420, doi: 10.1098/rsta.1904.0024.

27. Dirk Anton George Bruggeman, Berechnung Verschiedener Physikalischer Konstanten von Heterogenen Substanzen. I. Dielektrizitätskonstanten Und Leitfähigkeiten Der Mischkörper Aus Isotropen Substanzen, *Annalen Der Physik* 416 (1935): 636–64, doi:10.1002/andp.19354160802.

28. M. G. Moharam and T. K. Gaylord, Rigorous Coupled-Wave Analysis of Planar-Grating Diffraction, *J. Opt. Soc. Am.* 71, 7 (1981): 811–18, doi: 10.1364/JOSA.71.000811.

29. Jerzy Adam Dobrowolski, Daniel Poitras, Penghui Ma, Himanshu Vakil, and Michael Acree, Toward Perfect Antireflection Coatings: Numerical Investigation, *Appl. Opt.* 41 (2002): 3075–83, doi: 10.1364/AO.41.003075.

30. Jerzy Adam Dobrowolski, Optical Properties of Films and Coatings, in *Handbook of Optics: Fundamentals, Techniques, and Design* (New York: McGraw-Hill, 1994, pp. 41).

31. Khalid Askar, Blayne M. Phillips, Yin Fang, Baeck Choi, Numan Gozubenli, Peng Jiang, and Bin Jiang, Self-Assembled Self-Cleaning Broadband Anti-Reflection Coatings, *Colloids and Surfaces A: Physicochem. Eng. Aspects* 439 (2013): 84–100, doi: 10.1016/j.colsurfa.2013.03.004.

32. Kevin T. Cook, Kwadwo E. Tettey, Robert M. Bunch, Daeyeon Lee, and Adam J. Nolte, One-Step Index-Tunable Antireflection Coatings from Aggregated Silica Nanoparticles, *ACS App. Mater. Interfaces* 4 (2012): 6426–31, doi: 10.1021/am3020586.

33. William H. Southwell, Gradient-Index Antireflection Coatings, *Opt. Lett.* 8, 11 (1983): 584–6, doi: 10.1364/OL.8.000584.

34. Grant R. Fowles, *Introduction to Modern Optics,* 2nd Edition (New York: Dover Publications, 1975).

35. Jonathan Moghal, Johannes Kobler, Jürgen Sauer, James Best, Martin Gardener, Andrew A. R. Watt, and Gareth Wakefield, High-Performance, Single-Layer Antireflective Optical Coatings Comprising Mesoporous Silica Nanoparticles, *ACS App. Mater. Interfaces* 4, 2 (2012): 854–9, doi: 10.1021/am201494m.

36. Mehdi Keshavarz Hedayati and Mady Elbahri, Antireflective Coatings: Conventional Stacking Layers and Ultrathin Plasmonic Metasurfaces, A Mini-Review, *Materials* 9, 6 (2016): 497, doi: 10.3390/ma9060497.

37. Jinghua Sun, Xinmin Cui, Ce Zhang, Cong Zhang, Ruimin Ding, and Yao Xu, A Broadband Antireflective Coating Based on A Double-Layer System Containing Mesoporous Silica and Nanoporous Silica, *J. Mater. Chem. C* 3 (2015): 7187–94, doi: 10.1039/C5TC00986C.

38. Mikhail A. Kats, Romain Blanchard, Patrice Genevet, and Federico Capasso, Nanometre Optical Coatings Based on Strong Interference Effects in Highly Absorbing Media, *Nature Materials* 12, 1 (2012): 20–4, doi: 10.1038/nmat3443.

39. Chan Il Yeo, Hee Ju Choi, Young Min Song, Seok Jin Kang, and Yong Tak Lee, A Single-Material Graded Refractive Index Layer for Improving the Efficiency of III–V Triple-Junction Solar Cells, *J. Mater. Chem. A* 3 (2015): 7235–40, doi: 10.1039/C4TA06111J.

40. Sung Jun Jang, Young Min Song, Jae Su Yu, Chan Il Yeo, and Yong Tak Lee, Antireflective Properties of Porous Si Nanocolumnar Structures with Graded Refractive Index Layers, *Opt. Lett.* 36, 2 (2011): 253–5, doi: 10.1364/OL.36.000253.

41. Matthew M. Hawkeye and Michael J. Brett, Glancing Angle Deposition: Fabrication, Properties, and Applications of Micro- and Nanostructured Thin Films, *J. Vac. Sci. Technol. A* 25 (2007): 1317–35, doi: 10.1116/1.2764082.

42. Scott R. Kennedy and Michael J. Brett, Porous Broadband Antireflection Coating by Glancing Angle Deposition, *App. Opt.* 42, 22 (2003): 4573–9, doi: 10.1364/AO.42.004573.

43. Sameer Chhajed, Martin F. Schubert, Jong Kyu Kim, and E. Fred Schubert, Nanostructured Multilayer Graded-Index Antireflection Coating for Si Solar Cells with Broadband and Omnidirectional Characteristics, *Appl. Phys. Lett.* 93 (2008): 251108, doi: 10.1063/1.3050463.

44. Xing Yan, David J. Poxson, Jaehee Cho, Roger E. Welser, Ashok K. Sood, Jong Kyu Kim, and E. Fred Schubert, Enhanced Omnidirectional Photovoltaic Performance of Solar Cells Using Multiple-Discrete-Layer Tailored- and Low-Refractive Index Anti-Reflection Coatings, *Adv. Funct. Mater.* 23 (2013): 583–90, doi: 10.1002/adfm.201201032.

45. Sung Jun Jang, Young Min Song, Chan Il Yeo, Chang Young Park, and Jae Su Yu, Antireflective Property of Thin Film a-Si Solar Cell Structures with Graded Refractive Index Structure, *Opt. Express* 19 (2011): 108–17, doi: 10.1016/j.surfcoat.2010.08.131.

46. Volker Schmidt, Stephan Senz, and Ulrich Gösele, Diameter-Dependent Growth Direction of Epitaxial Silicon Nanowires, *Nano Lett.* 5 (2005): 931–5, doi: 10.1021/nl050462g.

47. Zhipeng Huang, Nadine Geyer, Peter Werner, Johannes De Boor, and Ulrich Gösele, Metal-Assisted Chemical Etching of Silicon: A Review, *Adv. Mater.* 23 (2011): 285–308, doi: 10.1002/adma.201001784.

48. Xuewen Geng, Meicheng Li, Liancheng Zhao, and Paul W. Bohn, Metal-Assisted Chemical Etching Using Tollen's Reagent to Deposit Silver Nanoparticle Catalysts for Fabrication of Quasi-Ordered Silicon Micro/Nanostructures, *J. Electron. Mater.* 40 (2011): 2480–5, doi: 10.1007/s11664-011-1771-1.

49. Jin-Young Jung, Zhongyi Guo, Sang-Won Jee, Han-Don Um, Kwang-Tae Park, Moon Seop Hyun, Jun Mo Yang, and Jung-Ho Lee, A Waferscale Si Wire Solar Cell Using Radial and Bulk p–n Junctions, *Nanotechnology* 21 (2010): 445303, doi: 10.1088/0957-4484/21/44/445303.

50. Jyh-Yuan Chen, Wui-Lee Chang, Chao-Kai Huang, and Kien Wen Sun, Biomimetic Nanostructured Antireflection Coating and Its Application on Crystalline Silicon Solar Cells, *Opt. Express* 19 (2011): 14411–19, doi: 10.1364/OE.19.014411.

51. Taiji Zhang, Yurong Ma, and Limin Qi, Bioinspired Colloidal Materials with Special Optical, Mechanical, and Cell-Mimetic Functions, *J. Mater. Chem. B* 1 (2013): 251–64, doi: 10.1039/c2tb00175f.

52. Yunfeng Li, Junhu Zhang, and Bai Yang, Antireflective Surfaces Based on Biomimetic Nanopillared Arrays, *Nano Today* 5 (2010): 117–27, doi: 10.1016/j.nantod.2010.03.001.

53. Hiroshi Toyota, Koji Takahara, Masato Okano, Tsutom Yotsuya, and Hisao Kikuta, Fabrication of Microcone Array for Antireflection Structured Surface Using Metal Dotted Pattern, *Jpn. J. Appl. Phys.* 40 (2001): L747–9, doi: 10.1143/JJAP.40.L747.

54. Yoshiaki Kanamori, Minoru Sasaki, and Kazuhiro Hane, Broadband Antireflection Gratings Fabricated upon Silicon Substrates, *Opt. Lett.* 24 (1999): 1422–4, doi: 10.1364/OL.24.001422.

55. Keiichiro Watanabe, Takayuki Hoshino, Kazuhiro Kanda, Yuichi Haruyama, and Shinji Matsui, Brilliant Blue Observation from a Morpho-Butterfly-Scale Quasi-Structure, *Jpn. J. Appl. Phys.* 44 (2005): L48–50, doi: 10.1143/JJAP.44.L48.

56. Young Min Song, Sung Jun Jang, Jae Su Yu, and Yong Tak Lee, Bioinspired Parabola Subwavelength Structures for Improved Broadband Antireflection, *Small* 6, 9 (2010): 984–7, doi: 10.1002/smll.201000079.

57. P. B. Clapham and M. C. Hutley, Reduction of Lens Reflexion by the "Moth Eye" Principle, *Nature* 244 (1974): 281–2, doi: 10.1038/244281a0.

58. K. Hadobás, S. Kirsch, A. Carl, M. Acet, and E. F. Wassermann, Reflection Properties of Nanostructure-Arrayed Silicon Surfaces, *Nanotechnology* 11 (2000): 161–4.

59. Zhaoning Yu, He Gao, Wei Wu, Haixiong Ge, and Stephen Y. Chou, Fabrication of Large Area Subwavelength Antireflection Structures on Si Using Trilayer Resist Nanoimprint Lithography and Liftoff, *J. Vac. Sci. Technol. B* 21 (2003): 2874–7, doi: 10.1116/1.1619958.

60. William H. Southwell, Pyramid-Array Surface-Relief Structures Producing Antireflection Index Matching on Optical Surfaces, *J. Opt. Soc. Am. A* 8 (1991): 549–53, doi: 10.1364/JOSAA.8.000549.

61. Matthias Geissler and Younan Xia, Patterning: Principles and Some New Developments, *Adv. Mater.* 16 (2004): 1249–69, doi: 10.1002/adma.200400835.

62. L. Jay Guo, Nanoimprint Lithography: Methods and Material Requirements, *Adv. Mater.* 19 (2007): 495–513, doi: 10.1002/adma.200600882.

63. Jun Hyuk Moon, Se Gyu Jang, Jong Min Lim, and Seung Man Yang, Multiscale Nanopatterns Templated from Two-Dimensional Assemblies of Photoresist Particles, *Adv. Mater.* 17 (2005): 2559–62, doi: 10.1002/adma.200501167.

64. Seung Man Yang, Se Gyu Jang, Dae Geun Choi, Sarah Kim, and Hyung Kyun Yu, Nanomachining by Colloidal Lithography, *Small* 2 (2006): 458–75, doi: 10.1002/smll.200500390.

65. Chih Hung Sun, Peng Jiang, and Bin Jiang, Broadband Moth-Eye Antireflection Coatings on Silicon, *Appl. Phys. Lett.* 92 (2008): 06112, doi: 10.1063/1.2870080.

66. Wei Lun Min, Amaury P. Betancourt, Peng Jiang, and Bin Jiang, Bioinspired Broadband Antireflection Coatings on GaSb, *Appl. Phys. Lett.* 92 (2008): 141109, doi: 10.1063/1.2908221.

67. Tsutomu Nakanishi, Toshiro Hiraoka, Akira Fujimoto, Satoshi Saito, and Koji Asakawa, Nano-Patterning Using an Embedded Particle Monolayer as an Etch Mask, *Microelectronic Engineering* 83 (2006): 1503–8, doi: 10.1016/j.mee.2006.01.193.

68. H. L. Chen, S. Y. Chuang, Chun-Hung Lin, and Y. H. Lin, Using Colloidal Lithography to Fabricate and Optimize Sub-Wavelength Pyramidal and Honeycomb Structures in Solar Cells, *Opt. Express* 15 (2007): 14793–803, doi: 10.1364/OE.15.014793.

69. Yunfeng Li, Junhu Zhang, Shoujun Zhu, and Bai Yang, Biomimetic Surfaces for High-Performance Optics, *Adv. Mater.* 21 (2009): 4731–4, doi: 10.1002/adma.200901335.

70. Junhu Zhang, Yunfeng Li, Xuemin Zhang, and Bai Yang, Colloidal Self-Assembly Meets Nanofabrication: From Two-Dimensional Colloidal Crystals to Nanostructure Arrays, *Adv. Mater.* 22 (2010): 4249–69, doi: 10.1002/adma.201000755.

71. Stephen J. Pearton and David P. Norton, Dry Etching of Electronic Oxides, Polymers, and Semiconductors, *Plasma Process. Polym.* 2 (2005): 16–37, doi: 10.1002/ppap.200400035.

72. Jia Zhu, Zongfu Yu, George F. Burkhard, Ching-Mei Hsu, Stephen T. Connor, Yueqin Xu, Qi Wang, Michael McGehee, Shanhui Fan, and Yi Cui, Optical Absorption Enhancement in Amorphous Silicon Nanowire and Nanocone Arrays, *Nano Lett.* 9 (2009): 279–82, doi: 10.1021/nl802886y.

73. Stuart Boden and D. M. Bagnall, Tunable Reflection Minima of Nanostructured Antireflective Surfaces, *Appl. Phys. Lett.* 93 (2008): 133108, doi: 10.1063/1.2993231.

74. Xudi Wang, Yanlin Liao, Bin Liu, Liangjin Ge, Guanghua Li, Shaojun Fu, Yifang Chen, and Zheng Cui, Free-Standing SU-8 Subwavelength Gratings Fabricated by UV Curing Imprint, *Microelectronic Engineering* 85 (2008): 910–13, doi: 10.1016/j.mee.2007.12.060.

75. Yoshiaki Kanamori, M. Ishimori, and Kazuhiro Hane, High Efficient Light-Emitting Diodes with Antireflection Subwavelength Gratings, *IEEE Photonics Technology Letters* 14 (2002): 1064–6, doi: 10.1109/LPT.2002.1021970.

76. Yoshiaki Kanamori, Hisao Kikuta, and Kazuhiro Hane, Broadband Antireflection Gratings for Glass Substrates Fabricated by Fast Atom Beam Etching, *Jpn. J. Appl. Phys.* 39 (2000): L735–7.

77. Philippe Lalanne and G. Michael Morris, Antireflection Behavior of Silicon Subwavelength Periodic Structures for Visible Light, *Nanotechnology* 8 (1999): 53–6, doi: 10.1088/0957-4484/8/2/002.

78. Young Min Song, Si Young Bae, Jae Su Yu, and Yong Tak Lee, Closely Packed and Aspect-Ratio-Controlled Antireflection Subwavelength Gratings on GaAs Using a Lenslike Shape Transfer, *Opt. Lett.* 34 (2009): 1702–4, doi: 10.1364/OL.34.001702.

79. Guoyong Xie, Guoming Zhang, Feng Lin, Jin Zhang, Zhongfan Liu, and Shichen Mu, The Fabrication of Subwavelength Anti-Reflective Nanostructures Using a Bio-Template, *Nanotechnology* 19 (2008): 095605, doi: 10.1088/0957-4484/19/9/095605.

80. Guoming Zhang, Jin Zhang, Guoyong Xie, Zhongfan Liu, and Huibo Shao, Cicada Wings: A Stamp from Nature for Nanoimprint Lithography, *Small* 2 (2006): 1440–3, doi: 10.1002/smll.200600255.

81. Chih-Hung Sun, Brian J. Ho, Bin Jiang, and Peng Jiang, Biomimetic Subwavelength Antireflective Gratings on GaAs, *Opt. Lett.* 33 (2008): 2224–6, doi: 10.1364/OL.33.002224.

82. Chih Hung Sun, Wei Lun Min, Nicholas C. Linn, Peng Jiang, and Bin Jiang, Templated Fabrication of Large Area Subwavelength Antireflection Gratings on Silicon, *Appl. Phys. Lett.* 91 (2007): 231105, doi: 10.1063/1.2821833.

83. Wei-Lun Min, Peng Jiang, and Bin Jiang, Large-Scale Assembly of Colloidal Nanoparticles and Fabrication of Periodic Subwavelength Structures, *Nanotechnology* 19 (2008): 475604, doi: 10.1088/0957-4484/19/47/475604.

84. Hongbo Xu, Nan Lu, Dianpeng Qi, Juanyuan Hao, Liguo Gao, Bo Zhang, and Lifeng Chi, Biomimetic Antireflective Si Nanopillar Arrays, *Small* 4 (2008): 1972–5, doi: 10.1002/smll.200800282.

85. Sen Wang, Xiao Zheng Yu, and Hong Tao Fan, Simple Lithographic Approach for Subwavelength Structure Antireflection, *Appl. Phys. Lett.* 91 (2007): 061105, doi: 10.1063/1.2767990.

86. Yasuhiko Kojima and Takahisa Kato, Nanoparticle Formation in Au Thin Films by Electron-Beam-Induced Dewetting, *Nanotechnology* 19 (2008): 255605, doi: 10.1088/0957-4484/19/25/255605.

87. Ching-Mei Hsu, Stephen T. Connor, Mary X. Tang, and Yi Cui, Wafer-Scale Silicon Nanopillars and Nanocones by Langmuir–Blodgett Assembly and Etching, *Appl. Phys. Lett.* 93 (2008): 133109, doi: 10.1063/1.2988893.

88. Wei-Lun Min, Bin Jiang, and Peng Jiang, Bioinspired Self-Cleaning Antireflection Coatings, *Adv. Mater.* 20 (2008): 3914–18, doi: 10.1002/adma.200800791.

89. Yi-Fan Huang, Surojit Chattopadhyay, Yi-Jun Jen, Cheng-Yu Peng, Tze-An Liu, Yu-Kuei Hsu, Ci-Ling Pan, et al., Improved Broadband and Quasi-Omnidirectional Anti-Reflection Properties with Biomimetic Silicon Nanostructures, *Nat. Nanotechnol.* 2, 12 (2007): 770–4, doi: 10.1038/nnano.2007.389.

90. Dianpeng Qi, Nan Lu, Hongbo Xu, Bingjie Yang, Chunyu Huang, Miaojun Xu, Liguo Gao, Zhouxiang Wang, and Lifeng Chi, Simple Approach to Wafer-Scale Self-Cleaning Antireflective Silicon Surfaces, *Langmuir* 25, 14 (2009): 7769–72, doi: 10.1021/la9013009.

91. Yun-Ju Lee, Douglas S. Ruby, David W. Peters, Bonnie B. McKenzie, and Julia W. P. Hsu, ZnO Nanostructures as Efficient Antireflection Layers in Solar Cells, *Nano Lett.* 8, 5 (2008): 1501–5, doi: 10.1021/nl080659j.

92. Brian G. Prevo, Emily W. Hon, and Orlin D. Velev, Assembly and Characterization of Colloid-Based Antireflective Coatings on Multicrystalline Silicon Solar Cells, *J. Mater. Chem.* 17 (2007): 791–9. doi: 10.1039/B612734G.

93. Srinivasan Venkatesh, Peng Jiang, and Bin Jiang, Generalized Fabrication of Two-Dimensional Non-Close-Packed Colloidal Crystals, *Langmuir* 23 (2007): 8231–5, doi: 10.1021/la7006809.

94. Henning Nagel, Armin G. Aberle, and Rudolf Hezel, Optimised Antireflection Coatings for Planar Silicon Solar Cells Using Remote PECVD Silicon Nitride and Porous Silicon Dioxide, *Prog. Photovolt. Res. Appl.* 7 (1999): 245–60, doi: 10.1002/(SICI)1099-159X(199907/08)7:4<245::AID-PIP255>3.0.CO;2-3

95. Charles Martinet, Victor Paillard, Aline Gagnaire, and J. Joseph, Deposition of $SiO_2$ and $TiO_2$ Thin Films by Plasma Enhanced Chemical Vapor Deposition for Antireflection Coating, *Journal of Non-Crystalline Solids* 216 (1997): 77–82, doi: 10.1016/S0022-3093(97)00175-0.

96. Parag Doshi, Gerald E. Jellison, Jr., and Ajeet Rohatgi, Characterization and Optimization of Absorbing Plasma-Enhanced Chemical Vapor Deposited Antireflection Coatings for Silicon Photovoltaics, *Appl. Opt.* 36, 30 (1997): 7826–37, doi: 10.1364/AO.36.007826.

97. C. C. Johnson, T. Wydeven, and K. Donohoe, Plasma-Enhanced CVD Silicon Nitride Antireflection Coatings for Solar Cells, *Sol. Energ.* 31 (1983): 355–8, doi: 10.1016/0038-092X(83)90133-0.

98. N. Marrero, R. Guerrero-lemus, B. González-díaz, and D. Borchert, Effect of Porous Silicon Stain Etched on Large Area Alkaline Textured Crystalline Silicon Solar Cells, *Thin Solid Films* 517 (2009): 2648–50, doi: 10.1016/j.tsf.2008.09.070.

99. Chih-Hung Sun, Wei-Lun Min, Nicholas C. Linn, Peng Jiang, and Bin Jiang, Large-Scale Assembly of Periodic Nanostructures with Metastable Square Lattices, *J. Vac. Sci. Technol. B* 27 (2009): 1043–7, doi: 10.1116/1.3117347.

100. Saleem H. Zaidi, Douglas S. Ruby, and James M. Gee, Characterization of Random Reactive Ion Etched-Textured Silicon Solar Cells, *IEEE Transactions on Electron Devices* 48 (2001): 1200–6, doi: 10.1109/16.925248.

101. Bum Sung Kim, Don Hee Lee, Sun Hee Kim, Guk Hwan An, Kun Jae Lee, Nosang V. Myung, and Yong Ho Choa, Silicon Solar Cell with Nanoporous Structure Formed on a Textured Surface, *J. Am. Ceram. Soc.* 92 (2009): 2415–17, doi: 10.1111/j.1551-2916.2009.03210.x.

102. Mohammad Malekmohammad, Mohammad Soltanolkotabi, Reza Asadi, M. H. Naderi, Alireza Erfanian, Mohammad Zahedinejad, Shahin Bagheri, and Mahdi Khaje, Combining Micro- and Nano-Texture to Fabricate an Antireflective Layer, *J. Micro/Nanolith. MEMS MOEMS* 11 (2012): 013011, doi: 10.1117/1. JMM.11.1.013011.

103. Asmiet Ramizy, Z. Hassan, Khalid Omar, Y. Al-Douri, and M. A. Mahdi, New Optical Features to Enhance Solar Cell Performance Based on Porous Silicon Surfaces, *Appl. Surf. Sci.* 257 (2011): 6112–17, doi: 10.1016/j. apsusc.2011.02.013.

104. Wei Han Huang, Chih Hung Sun, Wei Lun Min, Peng Jiang, and Bin Jiang, Templated Fabrication of Periodic Binary Nanostructures, *J. Phys. Chem. C* 112 (2008): 17586–91, doi: 10.1021/jp807290u.

105. Qin Chen, G. Hubbard, Philip Shields, Chaowang Liu, D. W. E. Allsopp, Wang Nang Wang, and S. Abbott, Broadband Moth-Eye Antireflection Coatings Fabricated by Low-Cost Nanoimprinting, *Appl. Phys. Lett.* 94 (2009), doi: 10.1063/1.3171930.

106. Seung-Yeol Han, Brian K. Paul, and Chih-Hung Chang, Nanostructured ZnO as Biomimetic Anti-Reflective Coatings on Textured Silicon Using a Continuous Solution Process, *J. Mater. Chem.* 22 (2012): 22906–12, doi: 10.1039/C2JM33462C.

107. Haesung Park, Dongheok Shin, Gumin Kang, Seunghwa Baek, Kyoungsik Kim, and Willie J. Padilla, Broadband Optical Antireflection Enhancement by Integrating Antireflective Nanoislands with Silicon Nanoconical-Frustum Arrays, *Adv. Mater.* 23 (2011): 5796–800, doi: 10.1002/adma.201103399.

108. Fang Jiao, Qiyu Huang, Wangchun Ren, Wei Zhou, Fangyi Qi, Yizhou Zheng, and Jing Xie, Enhanced Performance for Solar Cells with Moth-Eye Structure Fabricated by UV Nanoimprint Lithography, *Microelectronic Engineering* 103 (2013): 126–30, doi: 10.1016/j.mee.2012.10.012.

109. Martin A. Green, Keith Emery, Yoshihiro Hishikawa, and Wilhelm Warta, Solar Cell Efficiency Tables (Version 31), *Prog. Photovolt: Res. Appl.* 16 (2008): 61–7, doi: 10.1002/pip.808.

110. Ning-Ning Feng, Jurgen Michel, Lirong Zeng, Jifeng Liu, Ching-Yin Hong, Lionel C. Kimerling, and Xiaoman Duan, Design of Highly Efficient Light-Trapping Structures for Thin-Film Crystalline Silicon Solar Cells, *IEEE Trans. Electron Devices* 54 (2007): 1926–33, doi: 10.1109/TED.2007.900976.

111. Jihun Oh, Hao-Chih Yuan, and Howard M. Branz, An 18.2%-Efficient Black-Silicon Solar Cell Achieved through Control of Carrier Recombination in Nanostructures, *Nat. Nanotechnol.* 7 (2012): 743–8, doi: 10.1038/nnano.2012.166.

112. Hao Chih Yuan, Vernon E. Yost, Matthew R. Page, Paul Stradins, Daniel L. Meier, and Howard M. Branzm, Efficient Black Silicon Solar Cell with a Density-Graded Nanoporous Surface: Optical Properties, Performance Limitations, and Design Rules, *Appl. Phys. Lett.* 95 (2009): 123501, doi: 10.1063/1.3231438.

113. Fatima Toor, Howard M. Branz, Matthew R. Page, Kim M. Jones, and Hao Chih Yuan, Multi-Scale Surface Texture to Improve Blue Response of Nanoporous Black Silicon Solar Cells, *Appl. Phys. Lett.* 99 (2011): 103501, doi: 10.1063/1.3636105.

114. Hitoshi Sai, Homare Fujii, Koji Arafune, Yoshio Ohshita, Yoshiaki Kanamori, Hiroo Yugami, and Masafumi Yamaguchi, Wide-Angle Antireflection Effect of Subwavelength Structures for Solar Cells, *Jpn. J. Appl. Phys.* 46 (2007): 3333–6, doi: 10.1143/JJAP.46.3333.

115. Zhida Xu, Jing Jiang, and Gang Logan Liu, Lithography-Free Sub-100 nm Nanocone Array Antireflection Layer for Low-Cost Silicon Solar Cell, *Appl. Opt.* 51 (2012): 4430–5, doi: 10.1364/AO.51.004430.

116. Young Min Song, Ji Hoon Jang, Jeong Chul Lee, Eun Kyu Kang, and Yong Tak Lee, Disordered Submicron Structures Integrated on Glass Substrate for Broadband Absorption Enhancement of Thin-Film Solar Cells, *Solar Energy Materials and Solar Cells* 101 (2012): 73–8, doi: 10.1016/j.solmat.2012.02.013.

117. Young Min Song and Yong Tak Lee, Antireflective Nanostructures for High-Efficiency Optical Sevices, *SPIE Newsroom*, November 30, 2010.